Prediction of the lifespan of cement at a specific depth based on the coupling of geomechanical and geochemical processes for CO2 storage

Bagheri, M., Shariatipour, S. M. & Ganjian, E.

Original citation & hyperlink:
Bagheri, M, Shariatipour, SM & Ganjian, E 2019, 'Prediction of the lifespan of cement at a specific depth based on the coupling of geomechanical and geochemical processes for CO2 storage', International Journal of Greenhouse Gas Control, vol. 86, pp. 43-65.
https://dx.doi.org/10.1016/j.ijggc.2019.04.016

DOI 10.1016/j.ijggc.2019.04.016
ISSN 1750-5836

Publisher: Elsevier

Prediction of the Lifespan of Cement at a Specific Depth Based on the Coupling of Geomechanical and Geochemical Processes for CO_2 Storage

Mohammadreza Bagheri[1,*], Seyed M. Shariatipour[1], Eshmaiel Ganjian[2]

[1] Research Centre for Fluid and Complex Systems, Coventry University, Mile Lane, Coventry CV1 2NL, UK
[2] School of Energy, Construction and Environment, Built & Natural Environment Research Centre, Coventry University, Coventry CV1 5FB, UK
* Correspondence: bagherim@coventry.ac.uk

Abstract: The injection of carbon dioxide (CO_2) captured from combustion-based processes into underground formations is one of a number of plausible methods to reduce its release into the atmosphere and consequential greenhouse gas warming. Once the gas has been captured efficiently and effectively, depleted oil and gas reservoirs are seen as high potential candidates for carbon storage projects. However, legacy issues associated with a high number of oil and gas wells abandoned during the last few decades put the carbon capture and storage projects (CCS) at risk. These include any defects within the cement surrounding the well casing or for capping an abandoned well that can become unwanted CO_2 leakage pathways. To predict the lifespan of these cements due to exposure to CO_2-bearing fluids at the conditions found underground, the geochemical processes need to be coupled with the geomechanical changes within the cement matrix. In a viable CCS project for sequestering CO_2, the cement matrix should be capable of withstanding acidic environments formed by dissolution of CO_2 in brine for more than ten thousand years. This work aims at providing a framework to predict the behaviour of cement due to CO_2 exposure under reservoir conditions. The results show that the chemical reactions and geomechanical changes within the cement matrix can result either in its radial cracking or radial compaction. Both of these behaviours are investigated as possible phenomena which may affect the CO_2 leakage, and therefore the viability of the site for long term carbon storage.

Keywords: Well cement; CO_2 leakage; carbon capture and storage; cement alteration, cement lifespan

Graphical Abstract:

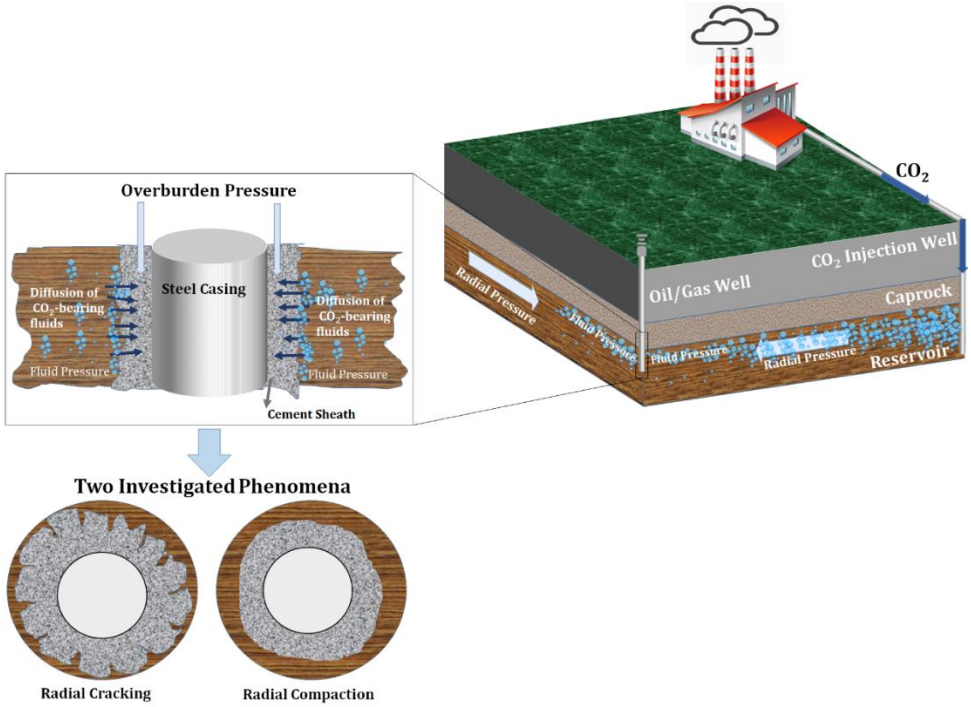

1 Introduction

The average global temperature is increasing due to the emission of anthropogenic greenhouse gases (Stocker et al., 2013). Carbon dioxide accounts for between 9-26% of the greenhouse gases (GHG) emission (Kiehl and Trenberth, 1997). One of the feasible strategies for decreasing the level of CO_2 in the atmosphere is to capture it at source, such as from power station flames and store it in underground formations. Depleted oil and gas reservoirs are potential candidates for CCS projects (Onoja and Shariatipour, 2018; Watson and Bachu, 2007). These types of underground formations are preferred because their structures have been well-characterised over different periods of the reservoir's life cycle.

These reservoirs are usually drilled extensively, and oil well cement has been used as a well lining or as a well plug once the well has been abandoned. One major problem is the high number of abandoned wells within these oil and gas reservoir, should the cement be a source of carbon dioxide leakage. For example, it is estimated that some 400,000 abandoned wells are located in the Alberta Basin in Canada, and more than one million are in Texas, USA (Celia et al., 2006). In Australia, this number is close to 10,000 (Davies et al., 2014). On the whole, from 1859 to 1994, around 3.2 million wells have been drilled in the USA of which 2.4 million have been left dry, inactive, or abandoned (Calvert et al., 1994). These types of oil and gas wells were generally cemented during the last century, but in some cases without compliance with the current standards. In fact, there was no universal regulatory system to control the quality of the cementing method.

Any defects within the rock-cement-casing assemblage could become a potential leakage path. Numerous experiments have been conducted to characterise different CO_2 leakage pathways, with a number of specific areas being cited, including the gap between the surrounding rock and the cement well sheath (Mason et al., 2013; Walsh et al., 2014a), the gap between the casing and the cement sheath (Bachu and Bennion, 2009; Carey et al., 2010), cracks within the cement sheath itself (Bachu and Bennion, 2009; Deremble et al., 2011; Huerta et al., 2013; Rimmelé et al., 2008), and percolation through the cement matrix (Barlet-Gouédard et al., 2009, 2007; Huerta et al., 2013; Rimmelé et al., 2008). In this paper, the term cement matrix is used interchangeably with cement sheath.

When CO_2 is injected deep into a target reservoir, it moves laterally just beneath the caprock before reaching any abandoned well, although there is not always a sudden change

from the reservoir formation to the caprock (Newell and Shariatipour, 2016; Onoja et al., 2019; Onoja and Shariatipour, 2018; Shariatipour et al., 2014; Seyed Mohammad Shariatipour et al., 2016). Therefore, sections of the well cement both across the reservoir and in the caprock may become exposed to CO_2-bearing fluids. CO_2 dissolves in brine as a ubiquitous phase within the depleted oil and gas reservoirs which results in the formation of carbonic acid. In the vicinity of the abandoned wells, the velocity of CO_2-bearing fluids is quite slow, therefore static conditions can be assumed (Brunet et al., 2016; Huerta et al., 2016; Huet et al., 2010; Shen et al., 2013). CO_2-bearing fluids penetrate through the cement matrix due to diffusion and advection phenomena (Druckenmiller and Maroto-Valer, 2005; Haghi *et al.*, 2017). This penetration results in the carbonation and the degradation of the cement matrix (Carey et al., 2010; Dijk and Berkowitz, 1999; Duguid and Scherer, 2010; Huet et al., 2010; Kutchko et al., 2007; Mainguy and Ulm, 2001; Walsh et al., 2013). Within a cylindrical cement matrix, which covers the steel casing of a wellbore, the CO_2 penetration results in the formation of a series of concentric zones each having differing characteristics (Abdoulghafour et al., 2016; Carey et al., 2007; Carroll et al., 2016; Corvisier et al., 2013; Duguid et al., 2011; Duguid and Scherer, 2010; Huerta et al., 2009; Hyvert et al., 2010; Raoof et al., 2012; Rimmelé et al., 2008). The mechanical properties of the altered zones are also changed compared to the unaltered ones (Mason et al., 2013). Generally, four main zones are expected to form within the cement matrix due to exposure to the CO_2-bearing fluids, including: an unaltered cement zone, a portlandite dissolution zone, a calcium carbonate precipitation zone (in this paper also referred to as the calcite precipitation zone), and an amorphous silica gel zone (Bagheri *et* al., 2018). Within the unaltered zone, generally, the pH is greater than 12 (Carey, 2013). In this range of pH, CO_3^{2-} is the predominant aqueous carbon ion. As the penetration of CO_2-bearing fluids continue the pH decreases, and the portlandite component in the cement matrix begins to dissolve, and at the same time, calcite precipitation is also expected (Liaudat et al., 2018). The portlandite dissolution increases the cement porosity (Carey, 2013). In the early stages of exposure to CO_2-bearing fluids, the rate of portlandite dissolution is higher than the calcite precipitation. Beyond this zone and close to the cement-brine interface, the calcite precipitation becomes dominant resulting in a reduction in the porosity (the process of calcite formation sometimes also referred to as carbonation). The calcium leaching from the calcium silicate hydrate (C-S-H) occurs within this zone and close to the cement-brine interface (Chen et al., 2004). The geochemical reactions lead to the conversion of C-S-H to an amorphous silica gel which leads to the highest porosity compared with other zones within the cement matrix (Figure 1). The re-dissolution of calcite within areas adjacent to the cement-brine interface also increases the porosity. The so-called degradation occurs close to the cement-brine interface which results in a porosity increase (Zhang and Bachu, 2011).

It was shown that the portlandite dissolution also results in a degradation in mechanical strength of the cement, although, in the layers closest to the cement-brine interface, the precipitation of the calcite may increase the mechanical strength (Ashraf, 2016; Nakano et al., 2014). In the immediate neighbourhood of the cement-brine interface, the cement degradation significantly contributes to a porosity increase and results in the degradation of mechanical strength (Brunet et al., 2013; Duguid and Scherer, 2010; Fabbri et al., 2009; Huerta et al., 2008; Kutchko et al., 2007; Lecampion et al., 2011; Walsh et al., 2014b; Zhang et al., 2013).

The cement sheath, generally, at the high pressure and temperature conditions found underground, undergoes geochemical and geomechanical changes. Both these processes may lead to the failure of the cement matrix resulting from either the creation of defects within the matrix or compaction/precipitation. The former phenomenon results in the formation of CO_2 leakage pathways, and the latter leads to so-called self-sealing behaviour preventing or slowing down the further movement of CO_2-bearing fluids into the cement matrix.

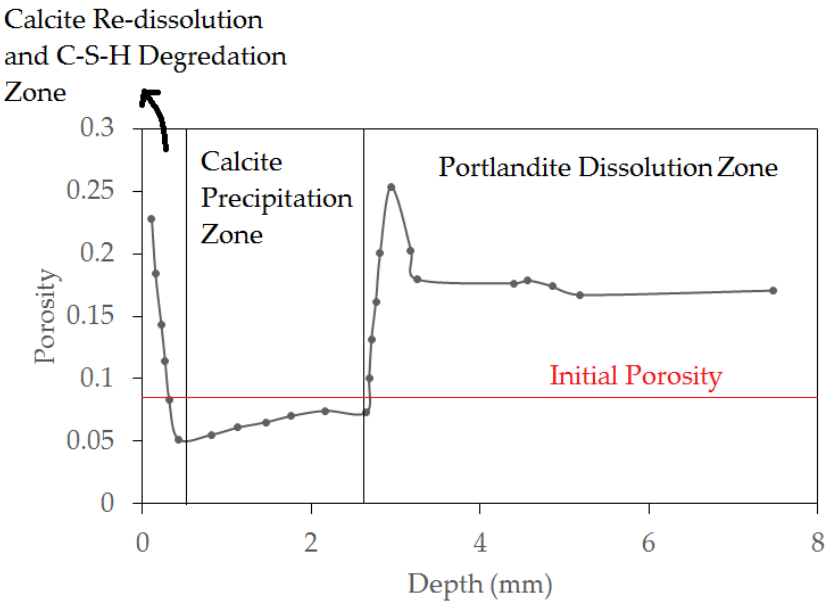

Figure 1. The porosity profile in a cement matrix exposed to CO_2-bearing fluids at 90°C and 280 bars over the period of four days against distance from the cement-brine interface on the left side to the inner parts of the cement on the right side (adopted from (Rimmelé et al., 2008)).

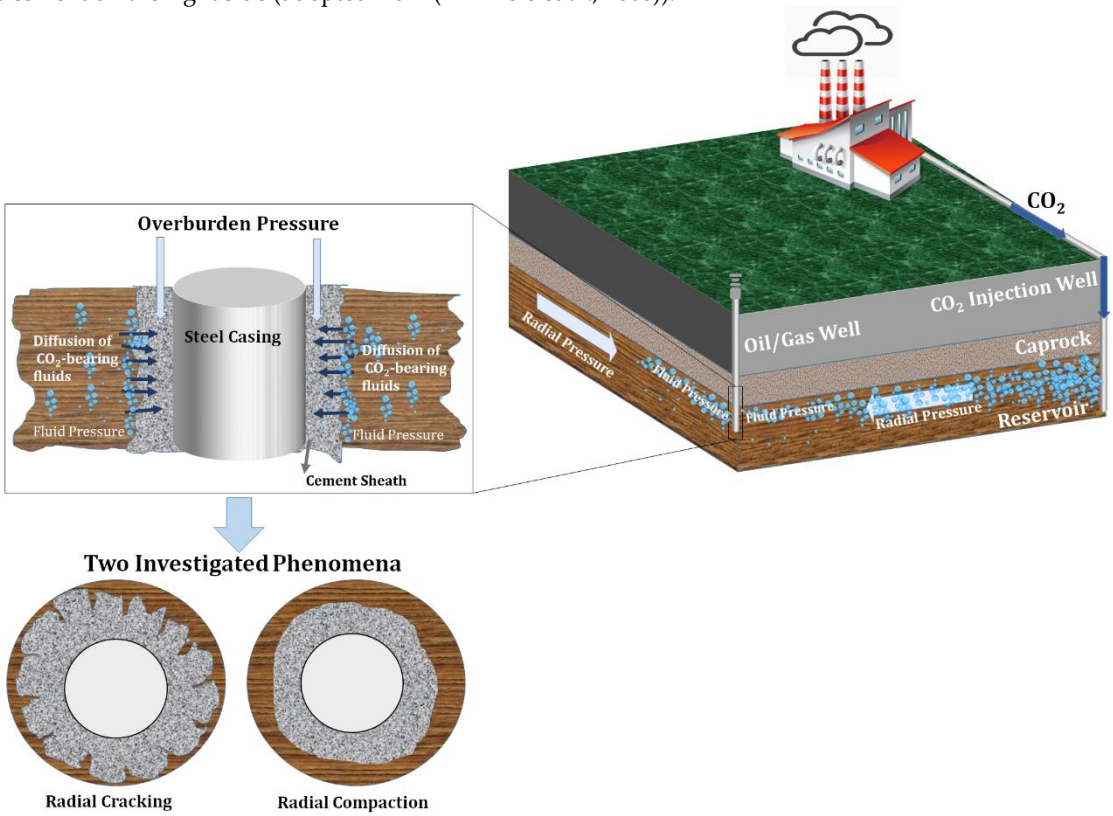

Figure 2. A simple illustration of the incurred pressures (or stresses) on the cement sheath, and the two main phenomena which may occur in the cement sheath.

Numerous attempts have been made to characterise cement carbonation. Generally, cement carbonation is considered as a linear diffusion phenomenon dominated by $d = kt^{0.5}$, where d is the depth of carbonation, t is time, and k is a constant which depends on the water saturation, relative humidity, CO_2 concentration, cement type, and other surrounding conditions (Ashraf, 2016; Phung et al., 2016; Rezagholilou et al., 2017; Šavija and Luković, 2016;

Silva et al., 2014; Ta et al., 2016). Nevertheless, the carbonation phenomenon is a complex process within the cement matrix followed by the degradation process in the presence of excess CO_2-bearing fluids. Therefore, a more precise modelling exercise needs the implementation to investigate the ongoing reactions within the cement due to CO_2-exposure (Barlet-Gouédard et al., 2009; Brunet et al., 2013; Kari et al., 2014; Kutchko et al., 2009, 2008, 2007; Liaudat et al., 2018; Peter et al., 2008; Zhang, 2016). The harsh conditions found underground, however, require the geomechanical changes of the cement to be accounted for.

The geomechanical integrity of well cements is also investigated at high-pressure and high-temperature conditions and for different failure modes identified in the literature (Xu et al., 2018; Zhang et al., 2015; Zhang and Wang, 2017). A qualitative measure of the wellbore instability based on a linear-elastic analysis using the failure criteria in the extensional and compressional regimes is provided by McLean and Addis (1990). Yu et al. (2003) model a more complex case by considering the chemical part for investigating the wellbore instability in shales. This work was undertaken by adding a solute diffusion to the governing equations to account for the fluxes of water and ions into and out of the shale. The integrity of the cement sheath was investigated using a thermo-poroelastic analytical approach by Gholami et al. (2016). It was shown that the fluid pressure reduction due to the fluid production and non-uniform stresses around the wellbore results in sand production and the deformation of the casing (Gholami et al., 2016b). A three-dimensional modelling of cement failure propagation due to the fluid leakage was conducted using a cohesive interface approach (Wang and Taleghani, 2014). It was found that large values of cohesive interface strength to a large extent can prevent the formation of failure cracks around the wellbore. The integrity of well cements under high-pressure conditions was modelled using a constitutive model for the cement sheath and a surface-based cohesive behaviour for the interfaces (Arjomand et al., 2018). They emphasized the importance of tensile strength and eccentricity which affect the distribution of stresses and the cracking index, respectively. Although these works inspect the geomechanical alteration of the well cements, they do not consider the effect of geochemical reactions on the mechanical properties of the cement matrix.

In this paper, the geochemical reactions are simulated using CrunchFlow code which was developed by Steefel et al. (2015). The geochemical alteration of the cement matrix is coupled with the geomechanical code developed by the authors to predict its lifespan. Overall, the work in this paper aims at providing a framework to predict the combined geochemical and geomechanical processes which a cement sheath is subjected to, at the conditions found in depleted oil and gas reservoirs. This helps in predicting the lifespan of a cement matrix exposed to CO_2-bearing fluids at a specific depth.

2 Methodology

This section illustrates the method which has been used to couple the geochemical alteration with the geomechanical processes within the cement matrix. Subsequently, the method of applying both the radial cracking and radial compaction phenomena in the simulations are represented, as the probable processes which may affect the integrity of the cement matrix with time.

2.1 Coupling the Geochemical Simulation with Geomechanical Simulation

Figure 3 shows the flowchart developed to simulate simultaneously the effect of geochemical and geomechanical changes within the cement matrix. Initially, CrunchFlow calculates the geochemical alteration within the cement matrix due to its exposure to CO_2-bearing fluids. The produced profile of porosity and mineral volume fractions are imported into the geomechanical simulation section. It is worth noting that the aqueous phase composition is assumed to remain unchanged throughout the calculation of the effects of geomechanical alteration within the cement matrix in each time step. The imposed stresses on the cement matrix result in the geomechanical changes. The cement matrix, in these

simulations, is 100% hydrated. This means that the cement matrix is at a stable state with a fixed mineral composition prior to being exposed to CO_2-bearing fluids. The carbonation process leads to the formation of different polymorphs of calcium carbonate affecting the stress state, and the stress state itself also impacts upon the crystallisation process. However, this process is not investigated here in order to decrease the complexity level governing the numerical solutions.

This geomechanical simulation produces a new profile of porosity and stresses. The Drucker-Prager failure criterion is used to predict the cement failure (details in Section 3.4). In the next step, the Drucker-Prager failure criterion will be compared to one in each cylindrical layer (Figure 5). This comparison reveals which layer is likely to fail. It should be noted that the whole cement sheath itself at a particular depth will also have a risk of failure if the overall Drucker-Prager failure criterion surpasses one.

After calculating the geomechanical-geochemical changes of the cement matrix properties, including the porosity, the mineral composition, and the chemical composition of the aqueous phase, the new produced profile of porosity and mineral volume fractions are imported into the CrunchFlow code at the next time step. This simulation progresses to predict the cement alteration at the next time step.

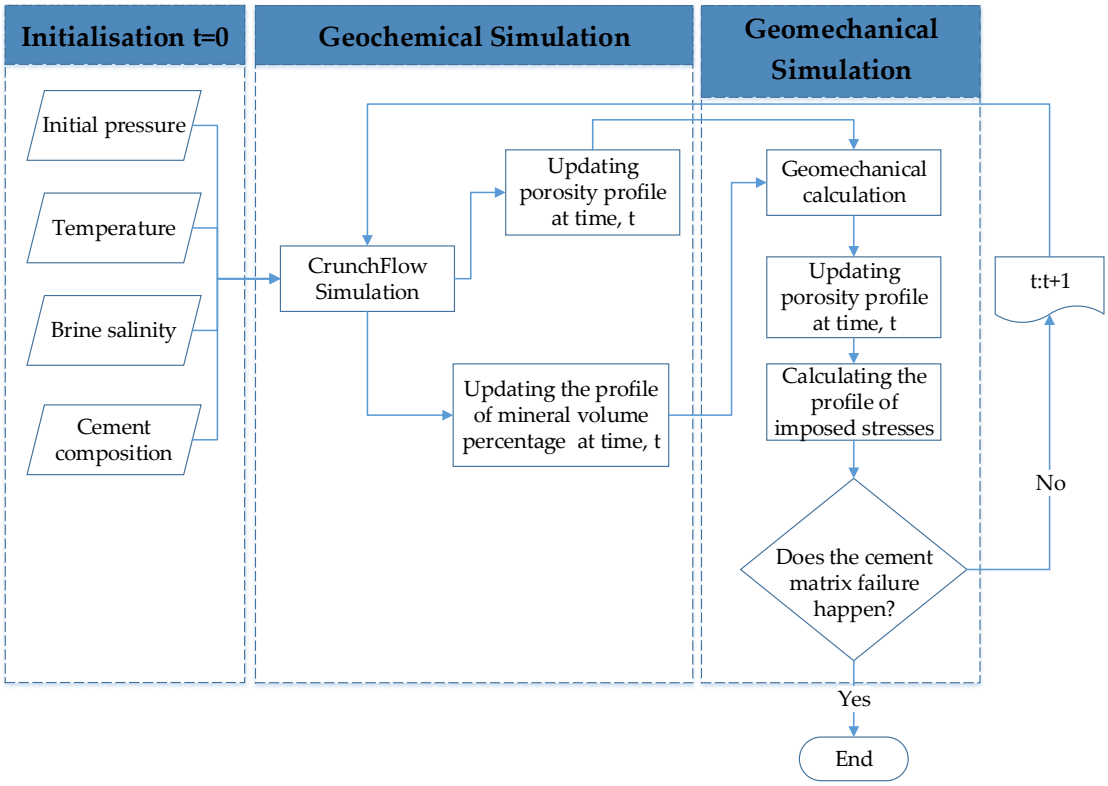

Figure 3. The flowchart for coupling the geochemical simulation with the geomechanical simulation.

2.2 Processes Governing Alterations in the Cement

The exposure of the cement matrix to CO_2-bearing fluids, at static conditions, activates the diffusion as the dominant process (Brunet et al., 2016; Huerta et al., 2016; Huet et al., 2010; Shen et al., 2013). The difference in the concentrations of the aqueous phase components within the pores of the cement sheath and the surrounding rocks initiates the process. As a consequence calcium starts to leach out the cement matrix and the penetration of carbon species into the cement matrix increases. It should be noted, however, that the carbonation reactions, i.e., the formation of calcite, within the cement matrix are a midway process which decreases the porosity and permeability and leads to an increase in the strength of the cement matrix

(Wolterbeek et al., 2016a, 2016b). Calculations in this paper verify this with an increase seen in the value of the Young's modulus of the carbonated layers.

The leaching of the calcium degrades the cement matrix. Typically, the outer layers have a high potential to be degraded due to their direct contact with lower-pH fluids. The next inner layers are the calcite precipitation zone, the portlandite dissolution zone, and the intact zone, respectively. The calcite zone, in between, acts as a barrier layer which limits the further penetration of CO_2-bearing fluids into the cement matrix.

If the Drucker-Prager failure criterion of the whole cement sheath becomes larger than one, the cement will fail. Otherwise, two states can exist: the first being the failure of the layers in which the Drucker-Prager failure criterion is larger than one. The failure can result in the formation of cracks within these layers. This phenomenon is simulated by producing a porosity of one within these areas which in this paper is referred to as the radial cracking process. Although the overall porosity of the cracked zones is less than one, the cracks within this zone provide high permeability pathways towards the inner layers of the cement matrix. In fact, the cracked zones also participate in the geochemical reactions, even though they are not strong enough to bear the effective stress. In this case, the permeability of the cracks is significantly higher, at least by five to six orders of magnitude, than the permeability of the un-cracked areas (Bachu and Bennion, 2009; Carey et al., 2010). The significant difference in the permeability of cracks and uncracked areas forces the fluid to flow through the high-perm cracks. Therefore, the low porosity of the un-cracked areas has a negligible impact on the calculations of fluid flux. Secondly, the radial stress on the loosened outermost layers may lead to a radial compaction process within this area. In fact, the compaction reduces the porosity within these areas to a fraction of its initial value, this phenomenon will be referred to as the radial compaction process. This process can limit or even prevent the penetration of CO_2-bearing fluids into the interior parts of the cement sheath. Imposing radial stresses can result in brittle faulting under low effective stresses, while the delocalization of cataclastic deformation within triaxially compressed cement matrices is associated with the porosity decrease (Wong and Baud, 1999).

If the cement matrix is considered analogous to mudrocks or shales, the cement matrix will exhibit a ductile behaviour under increased stress, becoming brittle under overstressed conditions. In the brittle condition, shear fractures show increased permeability, while in the ductile condition, the permeability decreases with increasing shear deformation (Nygård et al., 2006). Therefore, the brittle-ductile transition behaviour (Lubarda et al., 2002) of the cement matrix to a high level clarifies whether the radial cracking or radial compaction processes dominate in its alteration. However, this issue is not investigated in this paper.

The following formula is used to calculate the *in-situ* horizontal stress; the radial stress on the outer face of the cement sheath from the surrounding rocks will be a fraction of this value (Breckels and van Eekelen, 1982):

$$\sigma_r = 0.0053d^{1.145} + 0.46(P_c - P_{cn}), \qquad for\ d < 3500\ m. \tag{1}$$

where, d is depth in m, P_c and P_{cn} are the fluid pressure and the normal pore pressure in MPa, repectively. This relationship has been suggested for calculating the *in-situ* horizontal stress in sedimentary basins in the U.S. Gulf coast. However, the authors believe that under normal underground conditions the radial stress on the outer face of the cement sheath will be in the range of zero to the value obtained using Equation (1). The radial stress may change depending on the basin conditions. The basin formation in the vicinity of the cement sheath, throughout time, can expand laterally due to either tectonic displacements or creeping. Tectonic movements that put a significant shear stress on the cement sheath, have not been investigated here. This expansion tightens the cement sheath around the casing which leads to an increase in the radial stress. Table 1 summarises the parameters and their values which are used throughout the simulations.

Table 1. The general parameters used in all simulations

Parameter	Explanation	Assumed value
Pfluid	Fluid pressure	This is an average value representing the fluid pressure within the underground formations targeted for CCS projects, assumed to be equal to the hydrostatic pressure of brine with a density of 1 gr/cc
Routside	The outside radius of the casing (or inside radius of the cylindrical cement matrix)	88.90 mm (or a production casing of 7-inch outer diameter)
Rinside	Inside radius of the casing	80.85 mm (or a production casing of 6.366-inch inner diameter)
Ncement	Number of the radial grids within the cylindrical cement matrix	600
Nbrine	Number of the radial grids within the brine surrounding the cylindrical cement matrix	400
Δt	Time-step	10 days
t_{final}	The final time of the simulation	1810 days
Compressive strength parameters: c, m, and n in the following equation: $2ln(\sigma) = mln(1-\emptyset) - n\emptyset + c$, (2)	Equation (2) is the simplified form of the Equation (46) obtained from (Lian et al., 2011). To determine these parameters, the compressive strength of the cement matrix supposed to be 84.8 MPa at a porosity of 0.20 (Chindaprasirt et al., 2005).	$m = 5.96$ $n = -10.01$ $c = 12.21$
Pinside	The fluid pressure inside the casing. An abandoned well is considered with a column of 900 ft of mud with a density of 1.097 gr/cc (11 lb/gal) just above the reservoir-caprock interface (details are explained in Section 3.1)	2.95 MPa
$\emptyset_i$	Initial porosity of the cement matrix	0.15 (Brunet et al., 2013)

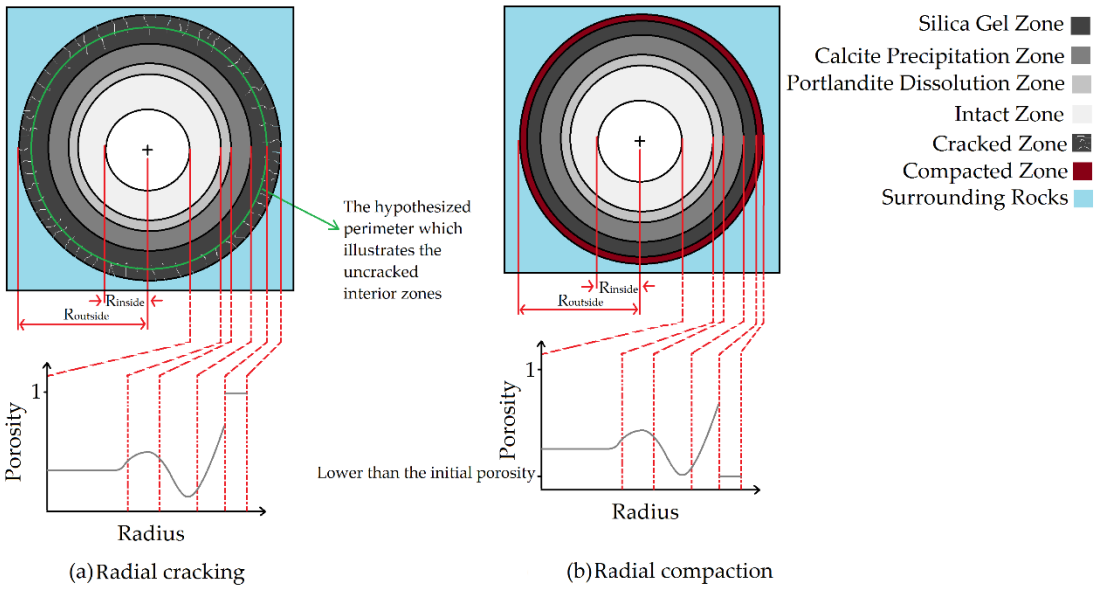

Figure 4. A cross-section of a cylindrical cement sheath with an inside radius of R_{inside} and outer radius of $R_{outside}$. (a) The radial cracking process in which the radius of the uncracked zone is changing throughout time due to the cement degradation; (b) the compaction process in which the outer layer is compacted due to the radial stress.

3 Geomechanics of Well Cement

This section investigates the geomechanical alterations in the properties of the cement matrix.

3.1 The Geomechanical Governing Formulas

A cement matrix is a porous rock which contains water within its pores. The pore water within the cement core is connected to the surrounding fluids. The concept of effective stress can be used to consider the effect of fluid pressure. This theory was applied to the estimation of rock strength (Hoek and Brown, 1997). However, some modifications were considered for low permeability porous media such as cement (Biot, 1955; Osipov, 2015). In this paper, it is assumed that the cement matrix stays within the linear elastic regime prior to the cement failing. The effective stress can be defined as follows:

$$\sigma_{effective} = \sigma - \alpha p, \tag{3}$$

where, $\sigma_{effective}$ is the effective stress, p is the fluid pressure, σ is the mean stress which is exerted on the cement matrix by external forces, and α is known as the Biot coefficient (Liu and Harpalani, 2014). The Biot coefficient value, α, is a complete definition of the interaction between the fluid pressure and solid grains. This coefficient depends on the external stress, the rock porosity, the compressibility of the solid grains and skeleton, consolidation type, and the ratio of consolidation to the cementation. The value of the Biot coefficient, α, changes from near zero to unity (Liu and Harpalani, 2014). The following formula was suggested for the value of Biot coefficient, α (Geertsma, 1957; Liu and Harpalani, 2014; Skempton, 1984).

$$\alpha = 1 - \frac{K}{K_s}, \tag{4}$$

where, K_s and K are the bulk modulus of grains and dry porous rock, respectively. As explained by Terzaghi (1943), the effective stress denotes the stress which is effective in moving soil or displacing soil. For an isotropic porous medium, the general strain tensor can be written as follows (Nur and Byerlee, 1971):

$$\varepsilon_{ij} = \frac{1}{2\mu}\left(\sigma_{ij} - \frac{1}{3}\delta_{ij}\sigma_{kk}\right) + \frac{1}{9K}\delta_{ij}\sigma_{kk} - \frac{1}{3H}\delta_{ij}p, \tag{5}$$

where, i , j show the principle directions and can be 1,2, or 3, σ_{kk} is defined as in Equation (6), σ_{ij} is the Cauchy stress tensor, δ_{ij} is Kroenecker's delta, K and μ are the bulk modulus of rock and shear modulus without the fluid pressure, respectively, and H is the effective modulus of the solid phase (Liu and Harpalani, 2014) to take into account the strain due to the fluid pressure. The following shows σ_{kk}:

$$\sigma_{kk} = \sigma_{11} + \sigma_{22} + \sigma_{33}, \quad (6)$$

and,

$$\alpha = \frac{K}{H}. \quad (7)$$

Therefore,

$$\varepsilon_{11} = \frac{1}{2\mu}\left(\sigma_{11} - \frac{1}{3}\sigma_{kk}\right) + \frac{1}{9K}\sigma_{kk} - \frac{1}{3H}p, \quad (8)$$

$$\varepsilon_{22} = \frac{1}{2\mu}\left(\sigma_{22} - \frac{1}{3}\sigma_{kk}\right) + \frac{1}{9K}\sigma_{kk} - \frac{1}{3H}p, \quad (9)$$

$$\varepsilon_{33} = \frac{1}{2\mu}\left(\sigma_{33} - \frac{1}{3}\sigma_{kk}\right) + \frac{1}{9K}\sigma_{kk} - \frac{1}{3H}p. \quad (10)$$

In a cylindrical system with radial symmetry, three normal stresses can be introduced as follows (σ_r, σ_z, and σ_θ acting on an element of the cement sheath which are shown in Figure 5 and Figure 6):

$$\sigma_{11} = \sigma_r, \quad (11)$$

$$\sigma_{22} = \sigma_\theta, \quad (12)$$

$$\sigma_{33} = \sigma_z. \quad (13)$$

where σ_r, σ_θ, and σ_z are stresses in r-direction, θ-direction and z-direction, respectively. In a cylindrical coordinate, the stress tensor will be as follows (Biot, 1955):

$$\sigma_{ij} = \begin{bmatrix} \sigma_r - \alpha p & \tau_{r\theta} & \tau_{rz} \\ \tau_{\theta r} & \sigma_\theta - \alpha p & \tau_{\theta z} \\ \tau_{zr} & \tau_{z\theta} & \sigma_z - \alpha p \end{bmatrix}, \quad (14)$$

τ_{ij} , in Equation (14) shows the shear stress in the plane normal to the i-direction and in the direction of j. This is a symmetric tensor, therefore, $\tau_{ij} = \tau_{ji}$. This equation shows that the fluid pressure affects the normal stress, but not the shear stress.

It is assumed that the cylindrical cement matrix is in contact with a high-pressure fluid at its perimeter. By considering λ, Lame's constant, as follows:

$$\lambda = K - \frac{2}{3}\mu. \quad (15)$$

where,

$$K = \frac{E}{3(1-2\nu)}. \quad (16)$$

and,

$$\mu = \frac{E}{2(1+\nu)}. \quad (17)$$

E is the modulus of elasticity or the Young's modulus, and ν is the Poisson's ratio.

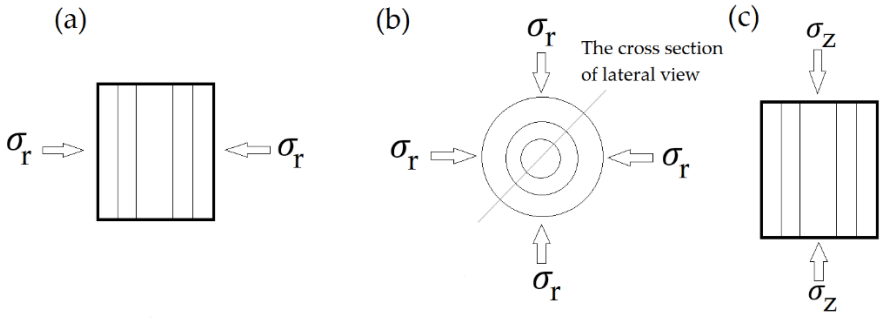

Figure 5. Illustration of the layers formed within a cylindrical cement matrix with respect to the imposed stresses; (a) layers are perpendicular to the radial stress; (b) the upper view of the cross-section which is influenced by radial stress; (c) lateral view of the layers which are parallel to the stress in the z-direction.

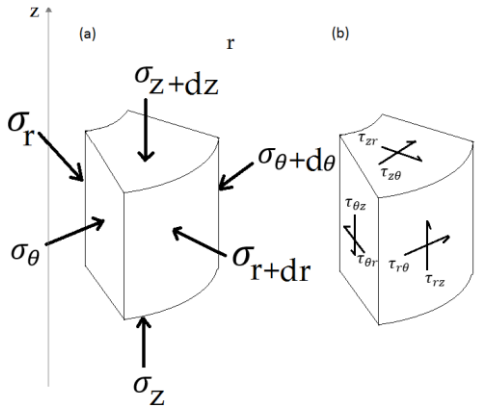

Figure 6. Stresses in cylindrical coordinates; (a) acting stresses in the r-direction, θ-direction and z-direction on the surfaces of the cement, and (b) shear stresses which are acting on the same cylindrical element.

Therefore, stresses can be rearranged as follows:

$$\sigma_r = \lambda(\varepsilon_r + \varepsilon_\theta + \varepsilon_z) + 2\mu\varepsilon_r + p\frac{K}{H}, \quad (18)$$

$$\sigma_\theta = \lambda(\varepsilon_r + \varepsilon_\theta + \varepsilon_z) + 2\mu\varepsilon_\theta + p\frac{K}{H}, \quad (19)$$

$$\sigma_z = \lambda(\varepsilon_r + \varepsilon_\theta + \varepsilon_z) + 2\mu\varepsilon_z + p\frac{K}{H}. \quad (20)$$

ε_r, ε_θ, and ε_z are strains in r-direction, θ-direction and z-direction, respectively.

The cylindrical cement matrix is assumed to be in the principal coordinate system in which the z-axis coincident with the centre line of the cylinder, such as Figure 6. To decrease the complexity of coupling the geochemical alterations with the geomechanical changes the following assumptions are applied to consider changes only in the r-direction, which can also be deuced from the plain strain assumption:

$$\frac{\partial u_z}{\partial r} = 0, \quad (21)$$

$$\frac{\partial u_r}{\partial z} = 0, \quad (22)$$

where, u_r and u_z are displacements in the in r-direction, and z-direction, respectively. From the symmetry, the following equations can be deduced:

$$u_\theta = 0, \quad (23)$$

$$\frac{\partial u_r}{\partial \theta} = 0, \quad (24)$$

$$\frac{\partial u_z}{\partial \theta} = 0, \quad (25)$$

where, u_θ is the displacement in the θ-direction. Based on Equations (21) to (25), the shear stresses on the cylindrical element will be zero. This means that u_z is only a function of z. Thus, the value of $\frac{\partial u_z}{\partial z}$ can be considered constant at a special cross-section perpendicular to the z-direction. The stress state of the cement sheath can be simplified to plain strain conditions applied widely to model vertical wells (Arjomand et al., 2018; Jo and Gray, 2010; Wang and Taleghani, 2014; Zhang et al., 2015). This means that the value of $\frac{\partial u_z}{\partial z}$ is zero (Sadd, 2005).

Strain-displacement relations,

$$\varepsilon_r = \frac{\partial u_r}{\partial r}, \quad (26)$$

$$\varepsilon_\theta = \frac{u_r}{r}. \quad (27)$$

From equilibrium equations, one can derive the following equations:

$$\frac{\partial \sigma_\theta}{\partial \theta} = 0, \quad (28)$$

$$\frac{\partial \sigma_r}{\partial r} = \frac{\sigma_\theta - \sigma_r}{r}, \quad (29)$$

$$\frac{\partial \sigma_z}{\partial z} = 0. \quad (30)$$

The stresses can be rewritten as follows:

$$\sigma_r = (\lambda + 2\mu)\frac{\partial u_r}{\partial r} + \lambda\left(\frac{u_r}{r}\right) + p\frac{K}{H}, \quad (31)$$

$$\sigma_\theta = (\lambda + 2\mu)\frac{u_r}{r} + \lambda\left(\frac{\partial u_r}{\partial r}\right) + p\frac{K}{H}, \quad (32)$$

$$\sigma_z = \lambda\left(\frac{\partial u_r}{\partial r} + \frac{u_r}{r}\right) + p\frac{K}{H}. \quad (33)$$

Equations (28) to (33) are the main governing equations which need to be solved to calculate σ_r, σ_θ, σ_z and u_r. To solve this system of equations at any cross-section perpendicular to the z-direction, Equations (29), (31), and (32) can be solved simultaneously. Equation (28) confirms that the obtained value for σ_θ is constant at all angles.

It should be recalled that due to radial change within the cylindrical cement matrix, the Young's modulus and the Poisson's ratio are functions of the radius, r, and the time, t.

$$E = E(r, t), \quad (34)$$

$$\nu = \nu(r, t). \quad (35)$$

This paper simulates the behaviour of the cement matrices in abandoned wells due to the effect of contact by dissolved CO_2. In this case, the abandoned wells are plugged using one of a number of plug placement techniques, in which the balanced plug method is the most common (Nelson, 1990). Texas state-wide plugging Rule 14 dictates that at least 100 ft of the hole (casing inside) and 10% of each 1,000 ft of the depth must be filled with plugs. Prior to the plugging procedure, the hole must be filled with mud with a minimum density of 9.5 lb/gal (Calvert et al., 1994). Therefore, if the CO_2 plume accumulates around the casing just beneath the caprock, the pressure inside the casing at that depth will be equal to the hydrostatic pressure of the fluid filling the casing. The maximum inside pressure will be equal to the static pressure of filling fluid with a height of 900 ft based on the Texas state-wide plugging Rule 14. Actually, the boundary conditions are highly dependent on the geometry of the cement-rock interface and the abandonment method. The following equations establish the boundary conditions:

$$\sigma_r = \sigma_R \text{ on }, r = R, \quad (36)$$

$$\sigma_r = p_{inside} \text{ on}, r = R_{inside}. \quad (37)$$

σ_R is the radial confining stress on the outer face of the cylindrical cement matrix at the radius of R. Equation (37) shows that the radial stress at the inner radius, R_{inside}, of the casing is equal to the fluid pressure, p_{inside}, in the casing at that depth.

The value of 0.25 is considered as being representative of the Poisson's ratio at different cylindrical layers (Chamrova, 2010; Constantinides and Ulm, 2004; Harsh et al., 1990; Velez et al., 2001; Wang and Subramaniam, 2011). The Young's modulus is a function of the porosity and the intrinsic properties of the cement matrix. The following equation characterises the change in Young's modulus against porosity (Phani and Niyogi, 1987):

$$E_r^t = {E_0}_r^t (1 - a\phi_r^t)^{n_r^t}, \quad (38)$$

The superscript t and the subscript r refer to terms time and radius, respectively. Parameters of a and n are material constants which are functions of the time and the radius. It can be assumed that at $\phi = 1$, the Young's modulus is zero (Lafhaj et al., 2006; Li et al., 2006). Thus, the changes in the porosity and the material constants can represent the changes in Young's modulus. It should be remarked that the constants a and n are unique for every porous solid.

3.2 Application to the Cement

CO_2-bearing fluids attacking the cement matrix results in the formation of four main zones (Carey et al., 2010; Choi et al., 2016; Corvisier et al., 2013, 2010; Iyer et al., 2017; Kutchko et al., 2008, 2007; Liaudat et al., 2018; Omosebi et al., 2016; Rimmelé et al., 2008). These zones include:

- The unaltered zone.
- The portlandite (CH) depleted zone (or the portlandite (CH) dissolution zone)
- The calcium carbonate precipitation zone. Although the formation of two polymorphs of Aragonite and Vaterite is also possible within this zone, calcite is the most metastable form of calcium carbonate (Carey, 2013; Corvisier et al., 2010; Wigand et al., 2009). This zone is also here referred to as the calcite precipitation zone.
- The silica gel zone where the degradation occurs due to both calcium leaching and the evolution of calcium silicate hydrate (C-S-H) (Bagheri et al., 2018; Chen et al., 2004).

The porosity remains unchanged within the unaltered zone. As Figure 1 shows, the value of porosity increases within the portlandite depleted zone and silica gel zone (Walsh et al., 2014a), while calcite precipitation leads to a porosity reduction (Barlet-Gouédard et al., 2007). Therefore, generally one could expect to see three major extremums on the porosity profile from the inner parts of a cement matrix to the cement-brine interface. These three extremums are associated with three main altered zones distinguished above within the reacted cement matrix. The first extremum in the porosity profile is due to the dissolution of CH in which the attack of CO_2-bearing fluids can be simulated by a decrease in the CH component and an increase in the porosity. The second extremum corresponds to the formation of the calcite, resulting in a porosity decrease. The last extremum is close to the cement-brine interface. Within this zone, calcite re-dissolution and C-S-H degradation occur resulting in the formation of the silica gel zone. Based on this observation, it is expected that the porosity value will increase here. The value of porosity in the silica gel zone is higher than both the porosity of the unaltered zone and the porosity extremum which is seen within the portlandite dissolution zone (Liaudat et al., 2018; Rimmelé et al., 2008).

Table 2. Young's modulus, E, of four main phases which are distinguished within the cement during the exposure to CO_2-bearing fluids.

Component	Young's modulus (GPa)	Reference
C-S-H	25.55	An average value is derived from (Chamrova, 2010; Constantinides and Ulm, 2007; Jennings et al., 2007)
CH	38.5	An average value is derived from (Chamrova, 2010; Constantinides and Ulm, 2004)
Calcite	70	An average value is derived from (Merkel et al., 2009)
Silica gel	159	It is assumed that the silica gel zone is composed of silicon and an average value is derived from (Hopcroft et al., 2010; Moner-Girona et al., 1999)

It is assumed that the cement matrix is a composite material. Therefore, the Young's modulus of this material can be represented by the Voigt or Reuss model (Liu et al., 2009; Zhu et al., 2015). The Voigt and Reuss models show the upper and lower bounds for the Young's modulus of the composite materials, respectively (Hill, 1952). To see the effect of microstructure on the elastic moduli, it can be deduced that the Young's modulus of the cement matrix lies somewhere between the lower and upper bounds (Carter and Norton, 2007). However, the Voigt model is more appropriate in representing the Young's modulus for a cement matrix. This is due to the direct effect of the Young's modulus of a newly formed mineral such as calcite on the overall Young's modulus. Therefore, the value of the Young's modulus, E, can be written in terms of four main components at the time, t, and the radius, r, which are predicted to occur within the cement composition prior to and during exposure to CO_2-bearing fluids as follows:

$$E_0(r,t) = E_{C-S-H} f_{C-S-H}(r,t) + E_{CH} f_{CH}(r,t) + E_{calcite} f_{calcite}(r,t) + E_{silica\ gel} f_{silica\ gel}(r,t), \quad (39)$$

where,

$$f_{C-S-H}(r,t) + f_{CH}(r,t) + f_{calcite}(r,t) + f_{silica\ gel}(r,t) = 1. \quad (40)$$

E_0 is Young's modulus of the cement matrix at the radius, r, the time, t, with a porosity of zero. E_{C-S-H}, E_{CH}, $E_{calcite}$, and $E_{silica\ gel}$ are the Young's moduli of C-S-H, portlandite, calcite, and silica gel, respectively, which are constant values, the average values being indicated in Table 2. f_{C-S-H}, f_{CH}, $f_{calcite}$, and $f_{silica\ gel}$ show the volume ratios of C-S-H, portlandite, calcite, and silica gel over the solid volume, respectively, which are also functions of the radius, r, and the time, t.

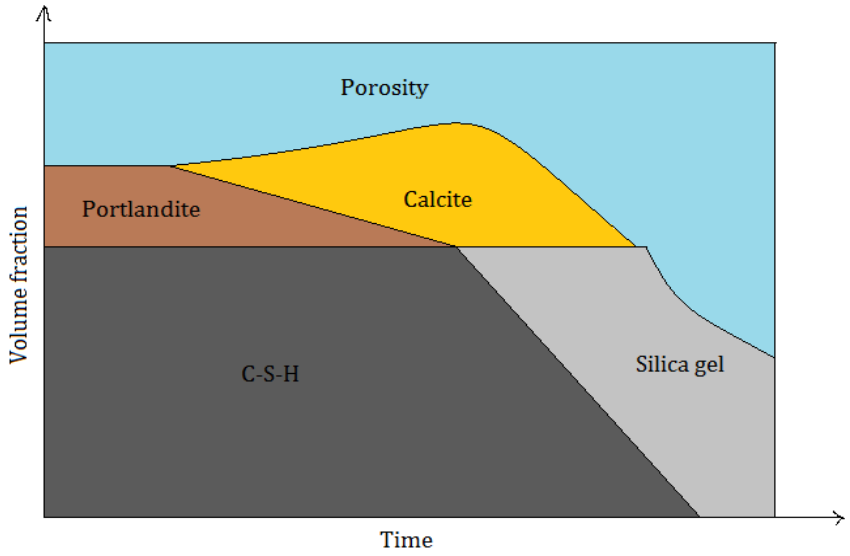

Figure 7. A simple illustration of the changes in the volume fraction of different presumed constituents of cement due to the exposure of CO_2-bearing fluids at a point within the cement matrix.

Figure 1 shows the alteration within the composition of the cement matrix from the cement-brine interface on the left side to the inner part of the cement matrix on the right side. It can be deduced that, in the areas close to the cement-brine interface, there is a negligible trace of portlandite and C-S-H. This zone is composed of silica gel which is an amorphous gel resulted from the evolution of C-S-H in the presence of high-CO_2 saturated fluids (Bagheri et al., 2018; Carey, 2013; Chen et al., 2004). The volume of silica gel itself also gradually decreases due to the dissolution in CO_2-bearing fluids. At deep locations within the cement matrix, portlandite dissolves in low-CO_2 saturated brine. The calcium cation which is freed from these areas starts diffusing out of the cement matrix. Prior to reaching the cement-brine interface, the calcium cation precipitates in the presence of a higher quantity of CO_3^{2-}. This process leads to an increase in the volume fraction of calcite. Moreover, the formation of calcite is accompanied by an increase in its volume due to crystallization (Hwang et al., 2018; Lesti et al., 2013; Šavija and Luković, 2016). These processes reduce the porosity and sometimes clog this intermediate zone. Within the portlandite dissolution zone, the C-S-H volume fraction is stable and throughout time portlandite is slightly converted to the calcite, as shown in Figure 7 (Liaudat et al., 2018).

The value of n in Equation (38) is a function of the mineral composition of the cement matrix. There is no explicit equation available in the iterature, to the authors' knowledge, to express n in terms of the mineral composition. Therefore, it should be calculated inversely from the Young modulus of a cement matrix. Mason et al. (2013) measured the Young's modulus, E, of altered layers and Rimmelé et al. (2008) investigated the porosity distribution within these altered layers. Table 2 shows the average Young's modulus of four main minerals occurring in cement matrices affected by CO_2-bearing fluids considering a porosity of zero. The calculation of n needs the mineral composition at the corresponding points to calculate E_0 using Table 2 and Equation (39). Therefore, at the points in which the Young's modulus, E, is measured by Mason et al. (2013), the mineral composition should be defined. It is estimated that the weight contribution of C-S-H and CH in the final composition of the cement after completing the hydration phase is 70% and 30 %, respectively (Nelson, 1990; Taylor, 1997). In fact, the CH contribution and other components are approximately 20% and 10%, respectively, but in this work, for simplicity, they are considered together. Considering an average density of 2.70 gr/cc for C-S-H (Allen et al., 2007; Jennings, 2000; Thomas et al., 2010) and a density of 2.26 gr/cc for CH leads to volume fractions of 67% and 33%, respectively.

In Table 3, it is assumed that in the middle of the portlandite dissolution zone, one-half of the portlandite volume is converted to calcite. At the middle of the calcite zone, the volume fraction of CH is negligible, and the volume fraction of the calcite is at its maximum of 0.33, while one-half of the total C-S-H is converted to silica gel. The silica gel zone, in Table 3, is also defined as a zone where silica gel is the only composing component. This table provides the value of n, in the last column on the right side, at four main points within a cement matrix exposed to CO_2-bearing fluids. The value of n at any other points should be interpolated based on these four main values using the mineral composition at that point. Actually, Table 3 will be used in simulations as a reference. The inverse distance weighting (IDW) method with a power parameter of four (Shepard, 1968) is applied to estimate the value of n. The interpolated value of n, thereafter, will be used in Equation (38) to compute E at that point.

Table 3. Calculating the average value of n in the in Equation (38) which is developed by Phani and Niyogi (1987).

Component / Zone	Volume fraction of minerals				Average porosity obtained from Figure 1	Associated depth (mm) obtained from Figure 1	Young's modulus (GPa) (Mason et al., 2013)	E_0	n
	C-S-H	CH	Calcite	Silica gel					
Unreacted zone	0.67	0.33	0	0	0.08	24.25	28.7	29.8	0.46
Portlandite dissolution zone	0.67	0.16	0.17	0	0.15	6	19.2	35.2	3.72
Calcite precipitation zone	0.33	0	0.33	0.34	0.07	1.5	20.9	85.6	19.43
Silica gel zone	0	0	0	1	0.35	0.1	9.8	159	6.47

3.3 Calculation of the Change in Porosity

The following equation expresses the change in the porosity due to imposing stresses on the cement matrix (Ghabezloo et al., 2008; Harrold, 2001; Liu and Harpalani, 2014):

$$\emptyset_{r_{new}}^{t} = \emptyset_{r_{old}}^{t} - \left(\frac{1-\emptyset_{r_{old}}^{t}}{K_r^t} - \frac{1}{K_{s_r}^{\ t}}\right)\left(\sigma_{m_r}^t - \alpha_r^t p\right). \quad (41)$$

Therefore,

$$\Delta\emptyset_{r_{geomechanical}}^{t} = -\left(\frac{1-\emptyset_{r_{old}}^{t}}{K_r^t} - \frac{1}{K_{s_r}^{\ t}}\right)\left(\sigma_{m_r}^t - \alpha_r^t p\right), \quad (42)$$

and,

$$K_r^t = \frac{E_r^t}{3(1-2\nu)}, \quad (43)$$

$$K_{s_r}^t = \frac{E_{0_r}^t}{3(1-2\nu)}. \quad (44)$$

where, $\emptyset_{r_{old}}^{t}$ is the porosity at the radius of r, and the time t, prior to the imposing the geomechanical changes. $\emptyset_{r_{new}}^{t}$ is the porosity after imposing the geomechanical changes. $\Delta\emptyset_{r_{geomechanical}}^{t}$ is the change in the porosity due to imposing stresses. $\sigma_{m_r}^t$ is the mean stress at the time, t, and the radius, r, and p is the fluid pressure. $K_{s_r}^{\ t}$ and K_r^t are the bulk modulus of grains and dry porous rock at the time, t, and the radius, r, respectively. The mean stress, $\sigma_{m_r}^t$, at the time, t, and the radius, r can be calculated as follows (Harrold, 2001):

$$\sigma_{m_r}^t = \frac{1}{3}(\sigma_r^t + \sigma_\theta^t + \sigma_z^t). \quad (45)$$

where σ_r^t, σ_θ^t, and σ_z^t are stresses in the r-direction, θ-direction , and z-direction, respectively, at the time t, and the radius, r.

The resulting porosity profile from the geochemical reactions will be added to the value of $\Delta\emptyset_{r_{geomechanical}}^t$ to show the coupled-effect of geochemical and geomechanical processes as formulated in Equation (66).

3.4 Prediction of Failure

The invasion of CO_2-bearing fluids into the cement matrix extensively affects the outmost layers, being close to the cement-brine interface. Chemical reactions change the mineral composition and porosity of these layers. With time, the inner parts of the cement matrix are also affected due to the diffusion of CO_2-bearing fluids. In this case, two states are plausible; firstly, a failure of the layers which are highly degraded, and secondly, the failure of the entire cement matrix. The former can lead to either the formation of cracks or the compaction of failed layers depending on the stress state. The latter illustrates that the entire cement matrix is no longer able to bear the mean effective stress, therefore the whole cement matrix fails.

In this paper, it is assumed that the cement matrix remains in the linear elastic zone prior to meeting the failure criterion. The cement matrix can be exposed to the extensional regimes particularly in the annulus of production/injection wells due to either the fluid flow pressure inside the casing or the temperature difference between the fluids inside the casing and the surrounding rock. This study investigates abandoned wells. This means that the cement matrix is generally at a steady state before being exposed to CO_2-bearing fluids. The assumptions, in this study, consider compressive radial stress. The geomechanical simulations also attest to the compressive nature of the vertical and hoop stresses. This means that a compressive regime is undergone during the calculations. Therefore a compressive criterion should be defined to show the cement failure. These models are based on the uniaxial compressive strength, which can be calculated as following (Lian et al., 2011):

$$\sigma_{ci_r}^t = B\sqrt{(1-\emptyset_r^t)^m e^{-n\emptyset_r^t}}, \quad (46)$$

where, $\sigma_{ci_r}^t$ and $\emptyset_r^t$ are the compressive strength and porosity at the time, t, and the radius, r. B is the compressive strength of the cement matrix at the porosity of zero which depends on the fracture energy of the cement matrix and as a consequence on its mineral composition, m and n are material constants which depend also on the cement composition. The value of the porosity changes throughout time due to geochemical reactions and imposing stress state on the cement matrix. The value of $\sigma_{ci_r}^t$ corresponds to a specific radius and time. To obtain a representative compressive strength for the whole cement matrix, an average value is calculated as follows:

$$\sigma_{ci}^t = \frac{1}{N}\sum_{i=1}^{N}\sigma_{ci_r}^t. \quad (47)$$

where, N is the number of the cylindrical layers of the cement sheath with a thickness of Δr at the time, t.

The internal friction angle, φ, and the cohesion, C, can be calculated based on the value of the compressive strength as follows (Rochette and Labossiere, 1996):

$$\varphi_r^t = sin^{-1}\left(\frac{3}{1+0.4\sigma_{ci_r}^t/\sqrt{3}}\right), \quad (48)$$

$$C_r^t = \left(\sigma_{ci_r}^t - 5\sqrt{3}\right)\frac{3-sin\,\varphi_r^t}{6\,cos\,\varphi_r^t}, \quad (49)$$

where, the subscript r stands for radius and superscript t stands for time. The internal friction angle and the cohesion can also be calculated for the whole cement matrix using σ_{ci}^t obtained from Equation (47) in Equations (48) and (49) instead of $\sigma_{ci_r}^t$.

The first invariant of the stress tensor, ${I_1}_r^t$, and the second invariant of the deviatoric stress tensor, $J_{2_r}^t$, at the time, t, and the radius, r, are as follows:

$$ {I_1}_r^t = \sigma_r^t + \sigma_\theta^t + \sigma_z^t, \quad (50) $$

$$ J_{2_r}^t = \frac{1}{6}((\sigma_r^t - \sigma_\theta^t)^2 + (\sigma_\theta^t - \sigma_z^t)^2 + (\sigma_r^t - \sigma_z^t)^2) + \tau_{r\theta}^2 + \tau_{rz}^2 + \tau_{\theta z}^2. \quad (51) $$

where, $\tau_{r\theta}$, τ_{rz}, and $\tau_{\theta z}$ are shear stresses which are equal to zero based on the plain strain assumption and the radial symmetry.

Octahedral shear stress, ${\tau_{oct}}_r^t$, and octahedral normal stress, ${\sigma_{oct}}_r^t$, at the time, t, and the radius, r, are as follows:

$$ {\sigma_{oct}}_r^t = \frac{{I_1}_r^t}{3}, \quad (52) $$

$$ {\tau_{oct}}_r^t = \sqrt{\frac{2}{3} J_{2_r}^t}. \quad (53) $$

Drucker-Prager criterion (Drucker and Prager, 1952) is used to define the failure envelope of the cement sheath under compression regime as following (McLean and Addis, 1990):

$$ {\tau_{DP}}_r^t = {\tau_{oct}}_r^t - m_r^t({\sigma_{oct}}_r^t - p_f), \quad (54) $$

where, ${\tau_{DP}}_r^t$ and m_r^t are the Drucker-Prager shear stress and a material parameter, respectively, at the time, t, and the radius, r. The latter can be calculated as follows (McLean and Addis, 1990):

$$ m_r^t = \frac{2\sqrt{2}\, sin\, \varphi_r^t}{3 - sin\, \varphi_r^t}. \quad (55) $$

The value of ${\tau_{DP}}_r^t$ obtained using Drucker-Prager criterion should be compared to the maximum shear stress which can be withstood by the cement matrix. McLean and Addis (1990) suggested the following:

$$ {\tau_0}_r^t = \frac{2\sqrt{2}\, C_r^t\, cos\, \varphi_r^t}{3 - sin\, \varphi_r^t}, \quad (56) $$

where, ${\tau_0}_r^t$, is the shear strength of the cement matrix which depends on its porosity, mineral composition, and structure. Therefore, the failure will occur at a radius of r when ${\tau_{DP}}_r^t$ becomes larger than ${\tau_0}_r^t$ which is represented by ratio η as follows:

$$ \eta = \frac{{\tau_{DP}}_r^t}{{\tau_0}_r^t}. \quad (57) $$

Although equations (48) to (57) were defined to predict the failure at a radius of r within the cement sheath, they can also be rewritten for the whole cement sheath using σ_{ci}^t instead of $\sigma_{ci_r}^t$, and the average stresses in each of principal directions of the cylindrical coordinate system. Although the outmost layers are highly prone to fail before the entire cement sheath, the reduction in the average strength of the cement sheath also exposes it to failure. Therefore, we need to check both the failure of the layers and the entire cement sheath to ensure which occurs first. The simulation moves forward through time to the collapse of the entire cement sheath.

3.5 Numerical Solution

Equations (29), (31), and (32) and boundary conditions in Equations (36), and (37) need to be solved simultaneously at each time step, Δt. The following shows the system of equations for calculating the displacement in the r-direction due to geomechanical changes. It is assumed that the radial thickness of the assemblage of cylindrical cement matrix and casing is discretized into N segments of Δr thickness. Therefore, $N + 1$ values of u_r are expected. u_1 refers to the radial displacement at the inside radius, R_{inside}, and u_{N+1} indicates the radial displacement at the outer face of the cement matrix or at the radius of $(R_{inside} + N\Delta r)$. For the radial displacement, the subscript i, and superscript t, will show the radius of $(R_{inside} + (i -$

1)Δr) and the time, t, respectively. For the stresses, the subscript, i, and superscript, t, will show the radius of ($R_{inside} + (i - 0.5)\Delta r$) and the time, t, respectively. By using the Euler method (Salamon, 1996), at the time, t, and the radius, r, and mathematical manipulation one can obtain the following system of equations:

	$(\lambda_i^t + 2\mu_i^t)\frac{u_{i+1}^t - u_i^t}{\Delta r} + \lambda_i^t\left(\frac{u_i^t}{r_i}\right) - \sigma_{r_i}^t = -p\alpha_i^t, \qquad i: 1, \dots, N,$	(58)
	$(\lambda_i^t + 2\mu_i^t)\frac{u_i^t}{r_i} + \lambda_i^t\left(\frac{u_{i+1}^t - u_i^t}{\Delta r}\right) - \sigma_{\theta_i}^t = -p\alpha_i^t, \qquad i: 1, \dots, N,$	(59)
	$\frac{\sigma_{r_{i+1}} - \sigma_{r_i}}{\Delta r} - \frac{\sigma_{\theta_i}^t - \sigma_{r_i}^t}{r_i} = 0, \qquad i: 1, \dots, N-1,$	(60)
	$2(\frac{\sigma_R - \sigma_{r_N}^t}{\Delta r}) - \frac{\sigma_{\theta_N}^t - \sigma_{r_N}^t}{r_N} = 0,$	(61)
	$\sigma_{r_1}^t\left(\frac{2}{\Delta r} + \frac{1}{R_{inside} + \frac{\Delta r}{2}}\right) - \sigma_{\theta_1}^t\left(\frac{1}{R_{inside} + \frac{\Delta r}{2}}\right) = p_{inside}\left(\frac{2}{\Delta r}\right),$	(62)

where

$$r_i = R_{inside} + (i - 0.5)\Delta r, \qquad i: 1, \dots, N. \tag{63}$$

4 Geochemical Simulation

The CrunchFlow code was used to simulate the geochemical changes within the cement due to the reactions (Steefel et al., 2015). This code has been used to simulate the energy, mass, and momentum conservation in the various literature (Brunet et al., 2016, 2013; Cao et al., 2015; Dávila et al., 2016; Zhang et al., 2013). The following equation expresses the change in the concentration of the components:

$$\frac{\partial(\phi C_j)}{\partial t} = \nabla.\left(D\nabla C_j\right) - \nabla\left(qC_j\right) + R_j \quad (j = 1,2,3, \dots n), \tag{64}$$

where ϕ is porosity, the term on the left-hand-side of Equation (64) indicates a change in the concentration, C_j, of the component j (mol/m^3), n is the number of involved components , the first, second, and third terms on the right side of Equation (64) stand for chemical species transport due to diffusion, advection, and reaction respectively, D is the combined diffusion-dispersion coefficient (m^2/s), q is the Darcy velocity ($m^3/(m^2.s)$), and R_j ($mol/(m^2.s)$) is the total reaction rate obtained from summing up rates of precipitation and dissolution of involved minerals.

Table 4. The initial concentrations of composing phases of the brine (Brunet et al., 2013).

		Cement Matrix	**Brine**
Aqueous phase species (mol/L)	CO_2(aq)	0.00	0.50
	Ca^{2+}	0.00	0.00
	Cl^-	0.17	0.17
	Na^+	As a conservative ion, its concentration is calculated based on charge balance.	0.17
	SiO_2(aq)	0.00	0.00
pH		13.00	2.90

Table 5. The initial volume factions of composing mineral phases of the cement matrix (Brunet et al., 2013).

		Cement Matrix	Brine
Mineral phase composition (Vol. %)	Portlandite	13.00	0.00
	Calcite	0.00	0.00
	C-S-H	72.00	0.00
	SiO_2(am)	0.00	0.00
Porosity (%)		15.00	100

Table 6. Reactions within the aqueous phase resulted from exposure to CO_2-bearing fluids (Brunet et al., 2013).

Aqueous phase reactions	Log (K_{eq})
$H_2O \leftrightarrow H^+ + OH^-$	-13.30
$CO_2(aq) + H_2O \leftrightarrow H^+ + HCO_3^-$	-6.09
$HCO_3^- \leftrightarrow H^+ + CO_3^{2-}$	-9.62
$CaCO_3(aq) \leftrightarrow Ca^{2+} + CO_3^{2-}$	-2.54
$CaCl^+ \leftrightarrow Ca^{2+} + Cl^-$	0.60
$CaCl_2(aq) \leftrightarrow Ca^{2+} + 2Cl^-$	0.59
$CaHCO_3^+ \leftrightarrow Ca^{2+} + HCO3^-$	-1.11
$CaOH^+ \leftrightarrow Ca^{2+} + OH^-$	-0.45
$NaCl(aq) \leftrightarrow Na^+ + Cl^-$	0.73
$NaHCO_3^-(aq) \leftrightarrow Na^+ + HCO3^-$	0.024

Table 7. Dissolution and precipitation reactions resulting from exposure to CO_2-bearing fluids (Brunet et al., 2013).

Reactions between the solid phase and the aqueous phase (precipitation and dissolution reactions)	**Log k** ($\frac{mol}{m^2.s}$)	**Log** (K_{eq})	**A** ($\frac{m^2}{gr}$)	α
$Ca(OH)_2(s) + 2H^+ \leftrightarrow Ca^{2+} + 2H_2O$	-6.20	21.05	16.50	0.18
$C\text{-}S\text{-}H(s) + 3.6H^+ \leftrightarrow 1.8Ca^{2+} + 7H_2O + SiO_2(am)$	-10.10	32.60	45.00	0.33
$CaCO_3(s) \leftrightarrow Ca^{2+} + CO_3^{2-}$	-6.10	-8.11	1.00	0.08
$SiO_2(am) \leftrightarrow SiO_2(aq)$	-10.00	-2.54	1.00	0.00

Table 8. Diffusion coefficients of species within the aqueous phase at 323.15 *K* (Brunet et al., 2013; Zhang et al., 2013).

Species	**D_0** (10^{-5} $\frac{cm^2}{s}$)
H^+	1.59
Ca^{2+}	1.36
OH^-	9.01
Cl^-	3.47
$HCO3^-$	2.02
CO_3^{2-}	1.63
$CO_2(aq)$	3.21
$SiO_2(aq)$	1.86
Na^+	2.27

Other species	1.00

The CrunchFlow code is based on the transition-state-theory to calculate the reaction rate for minerals. The included reactions corresponding to the minerals are assumed to be divided into two main groups, namely precipitation and dissolution reactions (Table 7). In fact, these two types of reaction affect the mineral volume fraction within the cement matrix. As a result, the porosity also changes based on Equation (65).

These types of reactions are generally considered to be kinetically controlled. This means that they are relatively slow, and a reaction rate constant (k) should be considered. The reactions within the aqueous phase are fast enough that they can be accounted for in Equation (64) based on their equilibrium constants (K_{eq}), which implies that they are controlled by the thermodynamics (Table 6) of the system. Table 6 and Table 7 summarise the assumed reactions occurring within the cement matrix and the brine in the pores of the cement matrix, respectively. A_0 is the specific surface area and α shows the dependency of reactions within the cement matrix upon H^+ activity.

Table 8 shows the pure diffusion coefficient (D_0) of the species within the pores of the cement matrix at 323.15 K. However, these coefficients are modified within the CrunchFlow code in order to calculate the effective diffusion coefficients using the porosity and cementation factor, which is 4.8. The diffusion process is responsible for the movement of species within the cement pores. Generally, in the vicinity of abandoned wells, the diffusion process dominates due to the static equilibrium conditions (Brunet et al., 2016; Huerta et al., 2016; Huet et al., 2010; Shen et al., 2013), while an advection process is more likely to be responsible for the renewal of CO_2-bearing fluids at the cement-brine interface in depleted oil and gas reservoirs (Abdoulghafour et al., 2016; Geloni et al., 2011; Huerta et al., 2016; Huet et al., 2010; Shen et al., 2013).

In this paper, it is assumed that in the vicinity of the abandoned wells the flow rate is negligible. Therefore, in this case, the static condition dominates the process and the advective phenomenon can be ignored. The porosity and the bulk volume of the cement matrix undergoes an alteration during its exposure to the CO_2-bearing fluids. This alteration occurs due to the geochemical and geomechanical changes within the cement matrix. Table 4 and Table 5 show the initial concentrations of contributed components within the cement matrix and the aqueous phase within the pores of the cement matrix.

The boundary conditions include zero-flux at the cement-casing interface and Dirichlet boundary condition which dominates at the cement-formation interface. It is assumed that the surrounding formation has no effect on the brine composition and it contains an infinite volume of brine compared to the pore volume of the cement matrix. This assumption results in the constant composition of the brine at the cement-formation interface. In fact, the advection phenomenon performs perfectly at the cement-formation interface and continuously brings refreshed brine with the composition presented in **Table 4** into contact with the cement matrix. Due to the low permeability of the cement matrix and zero-flux at the cement-casing interface, the diffusion phenomenon becomes the dominant process for the transport of the materials within the cement matrix. The initial composition of the mineral and aqueous phases are indicated in **Table 4** and **Table 5**. Therefore, with time, the composition of the mineral and aqueous phases in the cement matrix alters, although the aqueous composition of the brine at the cement-formation interface remains unchanged. These conditions are included in CrunchFlow importing file.

The porosity changes due to the chemical reactions and is updated at each time step as following:

$$\emptyset^t_{r_{geochemical}} = 1 - \sum_{m=1}^{N_m} V^t_{m_r}, \qquad (65)$$

N_m shows the number of mineral components which are present within the cement matrix, and $V_{m_r}^t$ shows the volume fraction of each mineral, m, at the radius, r, and time, t, although, it should be noted that this change is only due to chemical reactions. The porosity should be updated to account for the geomechanical alteration within the cement matrix. Therefore, one can calculate the final value of the porosity due to the geochemical and geomechanical changes as follows:

$$\emptyset_r^t = \emptyset_{r_{geochemical}}^t + \Delta\emptyset_{r_{geomechanical}}^t, \quad (66)$$

where $\emptyset_r^t$ is the porosity at the radius, r, and the time, t.

5 Verification of Methodology

The penetration depth of CO_2-bearing fluids into a cement matrix has been tracked for a period of one year by Kutchko et al. (2008). It was expected that the depth of the carbonation front follows Fick's second law. However, the result of the experiment was different, and the trend was found to fit by using the Elovich equation as follows (McLintock, 1967):

$$\frac{dx}{dt} = ae^{-bx}. \quad (67)$$

where, x is the penetration depth, t is the time, a and b are constants determined using the experiments. Nevertheless, this equation cannot be used to justify the trend that dominates the penetration depth within the cement matrix. The penetration depth is a function of the cement composition, the aqueous phase within the pore space, the stress state, and temperature. Therefore, it seems that the Elovich equation cannot be an appropriate candidate to capture the complex interactions that occur within the cement matrix due to the exposure to CO_2–bearing fluids. It is deduced that the radial cracking phenomenon is more likely to occur to simulate the dominant process, as the samples are surrounded by fluids and the confining stress is zero. Therefore, the radial cracking process is expected to occur more than the radial compaction one.

Figure 8 shows the penetration depth of the portlandite dissolution front due to the invasion of CO_2-bearing fluids into a cement matrix, as measured by Kutchko et al. (2008). In this simulation, the portlandite dissolution front is assumed to be a location in the r-direction where its volume fraction falls below 90% of its initial value. The portlandite dissolution front matches the experimental results after 60 days and the coefficient of determination (R^2) between 60 and 365 days is 0.99.

The penetration depth of the portlandite dissolution front is above and close to the calcite precipitation front prior to 90 days. It should be noted that in this simulation the calcite precipitation front is considered as a location in the r-direction where the volume fraction of calcite goes beyond 16%. With increasing time, from 90 to 365 days, the difference between the penetration depth of the calcite precipitation front and the portlandite dissolution front increases to about 0.1 mm. The reason can be found in the changes in the pH of the pore fluids within the cement matrix. The simulation calculates the pH penetration front as the location where the pH descends to below 95% of the pH value within the intact zone close the centre of the cement matrix. The value of the pH within the intact zone decreases from 13.00 to 12.74 during the first 100 days. In fact, exposing the cement matrix to CO_2-bearing fluids not only results in a large change in pH within the outer layers of the cement matrix, but also the inner layers are influenced by the CO_2 attack. The dissolution of portlandite is a strong function of the degree of acidity. It dissolves in the acidic brine ahead of the other components within the cement matrix (Liaudat et al., 2018). The pH within the intact zone decreases from 12.74 to 11.87 through 265 days, from day 100 to 365. Therefore, as Figure 8 shows, after 100 days the distance between the calcite precipitation front and the portlandite dissolution front increases. Simulations show that the calcite precipitation at the depth of 0.59 mm reduces the porosity to about 0.03. This phenomenon slows down the movement of the pH front, due to a decrease in the diffusion coefficient. The difference between the results of Kutchko et al. (2008) and the

penetration depth of the calcite precipitation and the portlandite dissolution may have been caused due to the sequential removing of the cement samples from a single high-pressure and temperature autoclave. Fluctuations in the vessel's pressure could create microfractures on the surface of the cement samples which facilitates the penetration of CO_2-bearing fluids into the inner parts of the cement matrix.

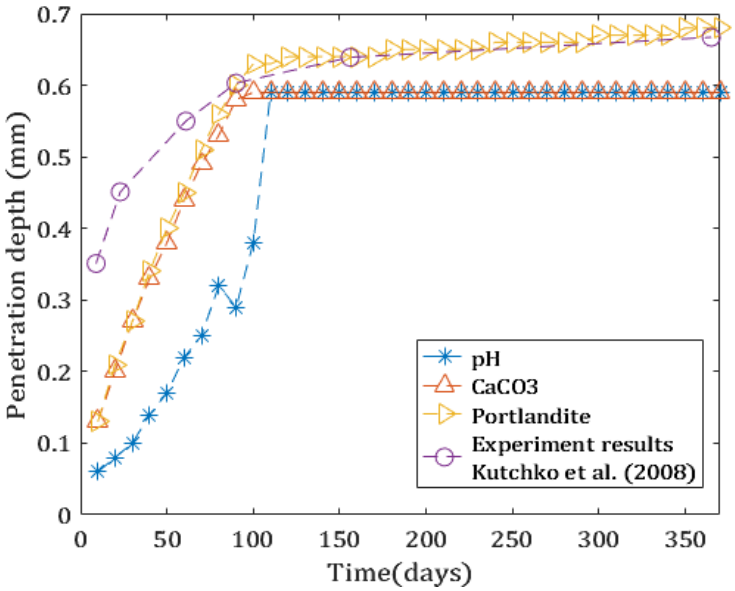

Figure 8. Prediction of the penetration depth into the cement matrix at the temperature of 50 ℃ in a CO_2-saturated brine pressurized to 30.3 MPa; brine is a 1% NaCl solution. Portlandite and C-S-H are considered as the main composing components of the cement matrix with the volume percentages of 13.5% and 75.2%, respectively, and a porosity of 11.3% prior to being exposed to CO_2-bearing fluids. The penetration depth is defined by Kutchko et al. (2008) as the deepest point in the cement matrix which is affected by CO_2-bearing fluids. Therefore, portlandite dissolution front is considered as the penetration depth.

The carbonation depth as a bright zone with decreased porosity was also measured by Liteanu and Spiers (2011). They applied a confining pressure of 30 MPa, and fluid pressure of 10 MPa on axially fractured cylindrical cement samples. The length and diameter of the cement samples were 17 mm and 35 mm, respectively. The fracture surfaces of water saturated samples were exposed to the supercritical CO_2 at a temperature of 80 ℃. The important aspect of this study was applying the confining stress at a static condition similar to the real conditions found in underground formations rather than only considering batch systems. The static condition is valid prior to the creation of a continuous leakage pathway around or within the cement sheath. In this case, the advection phenomenon will also affect the leakage pathways depending on the residence time and the initial aperture size of the fracture (Brunet et al., 2016; Iyer et al., 2017). To simulate the ingress of carbonation front within the cement matrix, the perimeter of the assumed cylindrical cement is considered to be 35 mm. The pH of the pore fluid and CO_2-saturated brine were considered to be equal to 3.0 and 13.0, respectively.

The predictions in Figure 8 and Figure 9 have been developed using the radial cracking process. There is no evidence reported relating to the compaction within the outer layers of the cement matrix close to the fracture surface (Liteanu and Spiers, 2011). Figure 9 shows the carbonation front penetration into the cement matrix which is shallower than the portlandite dissolution front similar to Figure 8. This occurs due to the high sensitivity of portlandite to pH change of the pore fluids. The simulation predicts the calcite precipitation front (or carbonation front in (Liteanu and Spiers, 2011)) precisely between 60 and 90 days, although, there is around 0.6 mm difference between the experimental results and the simulation prediction after ten days. This could be a result of the early compaction of the softened and crushed layers on the

fracture walls due to the fluid pressure and confining stress following fracturing. With increasing duration, these layers dissolve into the CO2-bearing fluids which facilitate the diffusion of the fluids into the cement matrix.

Overall, Figure 9 shows an approximation of the alteration of the cement in CO_2-rich environments considering the fracture wall as the surface of a cylindrical cement matrix. Therefore, although only a fraction of the fracture surface will be exposed to CO_2-bearing fluids, its impact on the penetration depth is not significant. This issue is important when the advection process contributes to the reactive transport. It is worth noting that the reaction rate constant of portlandite in this simulation is about one order of magnitude greater than in the experiments of Kutchko et al. (2008). The reason is based on the difference between the experiments' temperature. Indeed, the impact of temperature on the geochemical reactions within the cement is more effective than that of pressure (Omosebi et al., 2015; Rice, 2005).

To the authors' knowledge there is a dearth of information pertaining to experiments employing the tri-axial stress state during the cement exposure to CO_2-bearing fluids. Therefore, the validation of the radial compaction process needs further experiment. The cement undergoes alterations in the stress state from the time of it is set in underground formations. Moreover, it is pressurized by the surrounding rocks, which needs to be considered in any experiment. Generally, the method which is presented in this paper closely predicts the cement alteration, particularly during the longer time periods of the experiments when the effects of primary induced conditions seem to be reduced.

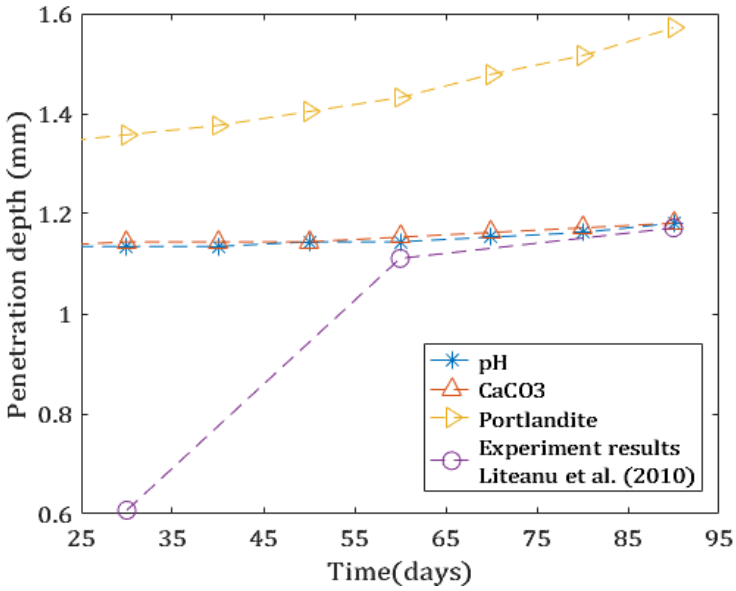

Figure 9. Comparison of the carbonation front ingress into the cement matrix obtained from the experiment in (Liteanu and Spiers, 2011) with the predicted penetration depth. Porosity is 0.36, and the volume percentages of portlandite and C-S-H is assumed to be 15% and 49%, respectively.

6 Results and Discussions

Two processes, namely radial cracking and radial compaction, were assumed to govern the alternation in the cement during exposure to CO_2 saturated brine. The lifespan of the cement affected by each of these two processes is predicted at different depths and under conditions found in underground formations. These investigations provide a framework illustrating the approximate failure time for a cement matrix in each of the dominant active processes after being exposed to CO_2-bearing fluids.

Determining whether the radial compaction process or radial cracking is the dominant actions depends on the underground conditions. The authors believe that the radial cracking process is active until the creep starts. In this period, and considering the normal underground

conditions, the cement is not significantly pressurized by its surrounding rock or fluids. With time, the radial compaction process becomes active due to either creeping or tectonic displacements. Therefore, the radial cracking seems to be active close to the inception of the process, which puts CCS projects at risk, while the activation of the radial compaction process at considerably further in time seems propitious though.

6.1 Radial Cracking

The cement sheath, which is cylinder-like, degrades radially with time due to the invasion of CO_2-bearing fluids. The reactions in this zone can be classified as carbonation and degradation, respectively. The carbonation process increases the cement strength (Ashraf, 2016; Omosebi et al., 2017, 2016; Šavija and Luković, 2016; Urbonas et al., 2016; Wolterbeek et al., 2016a), while degradation results in the weakening of the cement. The degraded cylindrical layers can be assumed to be similar to a sponge area surrounding the carbonated and the intact zones within the cement sheath such as Figure 4 (a). The probability of the radial cracking increases in conventional API oil well cements, although a low rate of carbonation was observed (Lesti et al., 2013).

To model this process, it is assumed that the failure within the outer layers leads to the formation of radial cracks. These cracks provide direct pathways for the invading fluid to migrate to the interior zones (Figure 4 (a)). Therefore, considering a porosity of one for the cracked outer layers can be a reasonable assumption. Gradually, the interior zones will also be affected by invading fluids. The radial cracking process will continue until the entire cement matrix fails. This section investigates the effects of the depth and the radial thickness of the cement sheath on its durability. The radial stress (σ_R) on the outer face of the cement sheath from the surrounding rocks is assumed to change between zero to the horizontal in-situ stress calculated by Equation (1). The depth is considered to vary from 800 to 2500 m which is the common range for the CO_2 storage projects (Herzog and Golomb, 2004; Rackley, 2017). In these simulations, the inside radius of the cement sheath is 88.9 mm (or a production casing with an outer and inner diameter of 7 and 6.366 inches, respectively). The ratio of the radial thickness of the cement sheath over its inside radius (t/r) changes from 0.06 to 2.22. For a borehole with an inner diameter of 9.10 inch, the value of t/r is 0.30. However, the borehole size is subject to change. In fact, the drilling operation affects the borehole walls; the precipitation of dislodged particles from the borehole walls reduces the borehole size. Meanwhile, the transfer of these particles can increase the borehole size at their initial places.

Based on the Equation (1), at a depth of 2075 m, the radial stress is assumed to be equal to 33.24 MPa. This value of this stress is equal to the horizontal *in-situ* stress under the normal underground conditions. It is considered that the radial stress can change from zero to 33.24 MPa depending on the surrounding environment adjacent to the well cement. The lifespan of the cement matrix at different ratios of t/r are shown in Figure 10, the radial stress in this figure is considered to be at 0%, 25%, 50%, 75%, and 100% of 33.24 MPa.

Figure 10 shows that with increasing t/r ratio from 0.06 to 2.22 the cement lifespan increases between 15 and 76 fold at different values of σ_R. Figure 10 is obtained from the extrapolation of curves in Figure 15 (referred to Appendix A.). The most stable state of the cement sheath occurs at σ_R of 8.31 MPa (or σ_R equal to 25% of the horizontal in-situ stress at the depth of 2075 m). At this σ_R, and increasing the t/r from 0.06 to 2.22, the cement lifespan increases from 122 years to more than 9380 years. The cement, at $a\ \sigma_R$ of 33.24 MPa, has the shortest lifespan compared to the lifespan of the cement at the other radial stresses, which increases from 53 to 1420 years as t/r is increased from 0.06 to 2.22. The lifespan of the cement sheath at a t/r of 0.3 is 158, 191, 150, 107 and 79 years at σ_R of 0, 8.31, 16.62, 24.93, and 33.24 MPa, respectively. If σ_R of zero is ignored in Figure 10, increasing the radial stress significantly reduces the lifespan of the cement sheath.

At a constant depth, the fluid pressure also remains constant in these simulations, because it is defined as a hydrostatic pressure due to the column of the fluid at that depth. The CO_2

concentration in brine is a function of the fluid pressure which generally increases with increasing the fluid pressure (Abbaszadeh and Shariatipour, 2018; Seyed M. Shariatipour et al., 2016). Thermodynamic rules (Duan and Sun, 2003; Spycher et al., 2003) determine the CO_2 concentration in brine which is expected at a specific fluid pressure. It should be noted that, in solids and liquids, chemical reactions are functions of the species concentration (Rice, 2005). This is based on negligible changes in the volume of solids and liquids with changes in the burden pressure. Therefore, after either the complete dissolution of CO_2 in brine or surpassing the maximum concentration predicted by thermodynamic rules, the fluid pressure will have no more direct impact on the chemical reactions (Bagheri et al., 2019). In Figure 10, the fluid pressure and temperature are above the critical pressure and temperature of CO_2, respectively, i.e., it completely dissolves in brine. The progress of chemical reactions is approximately equal at different σ_R in this figure, therefore, the stress state is considerably determinative of the cement lifespan.

If a σ_R of zero is ignored, increasing the radial stress results in an increase in the effective stress. The layers which are adversely affected by CO_2-bearing fluids will be susceptible to cracking. At a σ_R of zero, the cement matrix is only subjected to fluid pressure and consequently, other stresses are produced as a reaction to this pressure.

The cement matrix, during early days after being exposed to CO_2-bearing fluids, shows a gradual increase in the porosity value. This is due to the primary dissolution of CH at each point within the cement matrix. In fact, CH is highly sensitive to the pH. Figure 11 (a) shows a slight increase in the value of the porosity during the first 110 days after exposure to CO_2-bearing fluids. This trend is seen in deep areas of all cement sheath with different thicknesses. After 110 days, the porosity shows a smooth decrease which illustrates the impact of imposed stresses.

At a t/r of 0.06 and 2.22, the porosity profile of a layer at a radial distance of 22.2 mm towards casing from the calcite precipitation zone is shown in Figure 11 (a) and (b), respectively. Figure 11 (a) simply shows that the porosity at σ_R of zero is lower than for the other radial stresses. This means that at low ratios of t/r and zero σ_R the cement matrix lasts a longer period of time. In Figure 11 (a), by ignoring zero σ_R, the porosity value increases with increasing the radial stress. From this, it can be deduced that the lifespan of the cement matrix is shorter at higher radial stresses.

In comparison to Figure 11 (a), Figure 11 (b) shows that the layer with the same distance from the calcite precipitation zone is more affected by CO_2-bearing fluids, with around a 0.14 increase in porosity. This reveals that at higher ratios of t/r the diffusion process brings an increased amount of carbon species coming in contact with inner parts. The higher porosity of the calcite precipitation zone at higher ratios of t/r allows deeper diffusion of carbon species in comparison to low ratios of t/r (Figure 12). Although at higher ratios of t/r a large zone shows a significant increase in the porosity, the thickness of this zone is not comparable to the whole radial thickness of the sheath. Moreover, at high ratios of t/r, deeper zone represents a porosity profile such as Figure 11 (a). If σ_R of zero is considered as an exception, with increasing t/r the lifespan of the cement sheath increases and the lifespan of the cement matrix is still shorter at higher radial stresses.

In Figure 10, at σ_R of zero, the pore walls of the cement matrix are under fluid pressure without any imposed radial stress. In this case, they undergo an extensional regime. However, simulations show that the fluid pressure within the pores of the cement matrix results in the compressive stresses both in the θ-direction and the z-direction. The stress in the r–direction is tensional where its magnitude is not comparable with the two other stresses. For a time period of 1810 days which is simulated in this paper, the minimum effective stress at the pore walls of the cement matrix does not fall below the tensile strength. Therefore, the Drucker-Prager criterion defined in this paper for the compressional regime is also used to illustrate the trend of the combined impact of stresses at σ_R of zero. Based on the low tensional strength of the

cement matrix (10-15% of its compressive strength (Arıoglu et al., 2006)), there is a high potential for tensile failure due to the fluid pressure. At σ_R of zero and low ratios of t/r, the average specific surface area of pores is not as large as at high ratios of t/r which can be understood from Figure 11. Therefore, at σ_R of zero and high ratios of t/r the average force which is acting on the pore walls of the cement matrix is high which leads to a shorter lifespan of the cement matrix in comparison to non-zero radial stresses. The fact is that the order of the cement lifespan which is seen in Figure 10 will remain the same at other initial values of the porosity for non-zero radial stresses. However, the relative position of the cement lifespan for σ_R of zero will change depending on the initial porosity and the mineral composition of the cement matrix.

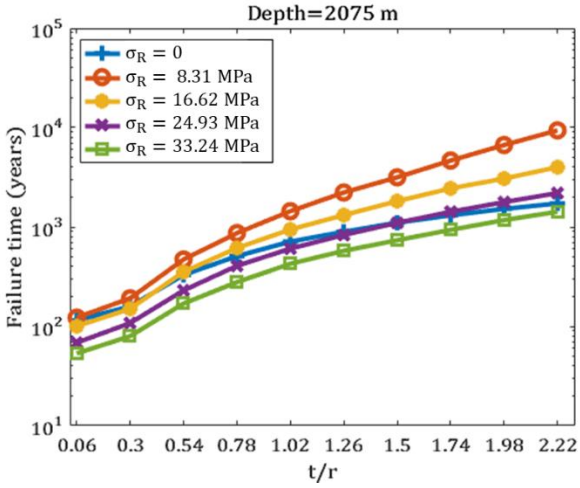

Figure 10. The failure time of the cylindrical cement matrices at the depth of 2000 m vs. the radial cement thickness over its inside radius (t/r) at the different radial stresses (σ_R) while the radial cracking process is active.

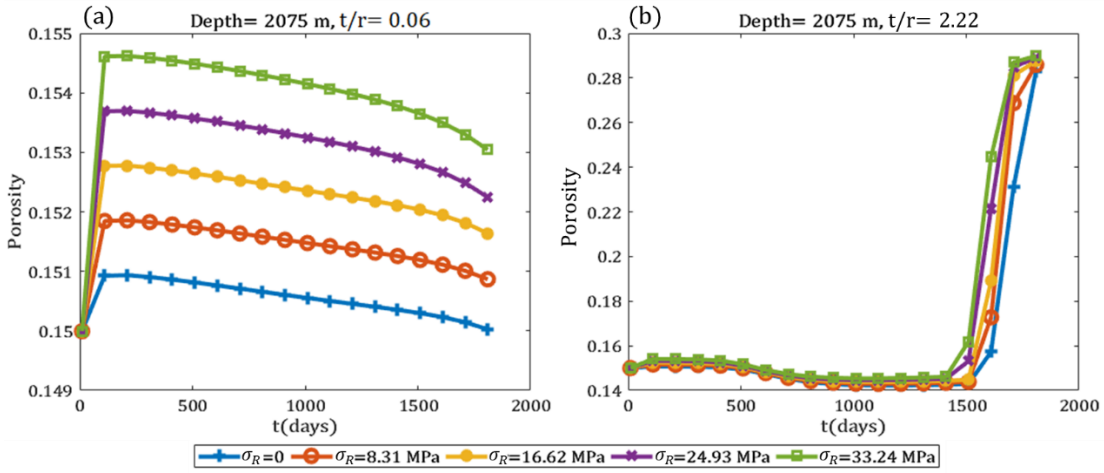

Figure 11. The porosity profile at a distance of 22.2 mm from the calcite precipitation zone towards casing, the radial cracking process is active, (a) at t/r of 0.06 and (b) at t/r of 2.22.

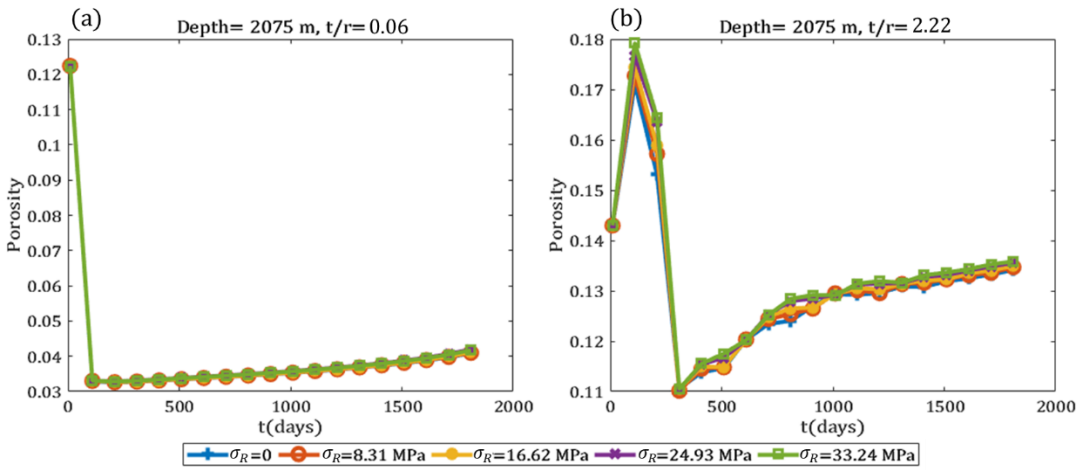

Figure 12. The porosity profile of calcite precipitation zone. The zone with the highest volume fraction of calcite is considered as the calcite precipitation zone, the radial cracking process is active, (a) at t/r of 0.06 and (b) at t/r of 2.22.

Decreasing the depth by 1700 m from 2500 to 800 m, leads to a five to six times increase in the cement lifespan, as shown in Figure 13. This figure is obtained from the extrapolation of curves in Figure 16 (referred to Appendix A.). As in Figure 10, it is also confirmed in Figure 13 that increasing the ratio of t/r from 0.06 to 2.22 results in around 25 times increase in the cement lifespan. At shallower depths, the radial stress is lower compared to deep locations, therefore, the effective stress is not comparable with the compressive strength of the cement matrix. It implies that the cement matrix can endure being exposed to CO_2-rich environments for longer periods of time. This can be advantageous because shallower depths can prevent the upward movement of CO_2-bearing fluids after the primary leakage through deeper well cements. In fact, it can exponentially delay the CO_2 leakage to the Earth's surface, in a longer timeframe than that predicted in Figure 13.

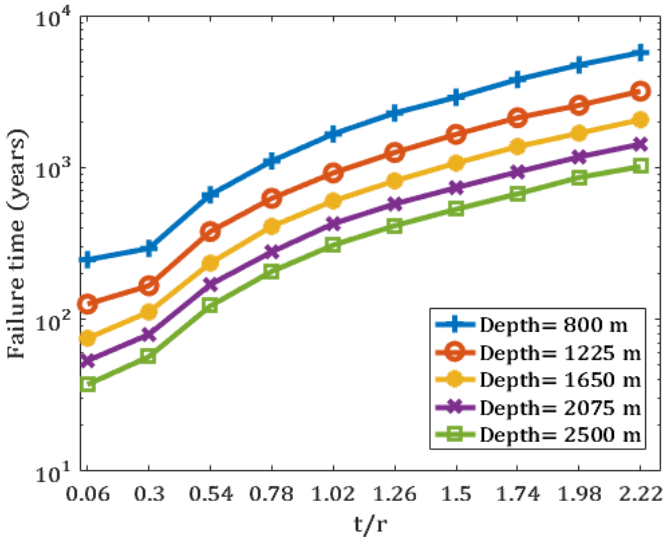

Figure 13. The failure time of the cylindrical cement matrices vs. the radial cement thickness over its inside radius (t/r) at the different depths while the radial carking process is active; the radial stress is calculated using Equation (1) at different depths.

6.2 Radial Compaction

At high radial stresses, the radial cracking process can be interpreted as the collection of dislodged particles surrounding the inner parts of the cement sheath. Although this zone is under radial stress from the surrounding rocks, the newly formed zone is similar to high

porosity clastic rocks. However, the probability of radial cracking is higher at low radial stresses. In fact, high radial stresses overcome the strength of the outmost layers of the cement sheath highly affected by CO_2-bearing fluids. In this case, the radial stress compacts the outer degraded zones. In fact, these layers will no longer be strong enough to withstand the radial stress which results in their compaction (Figure 4 (b)) (Carroll et al., 2017). It can be shown that in this state the degraded layers are perpendicular to the radial stress (Figure 5). The Young's modulus will be close to its lower limit in the radial direction based on the Reuss model (Liu et al., 2009; Zhu et al., 2015). Therefore, it is expected that the porosity value within these layers decreases to a fraction of its initial value. This process is simulated by considering a degree of reduction in the porosity when a layer fails based on Drucker-Prager criterion. The value of the porosity is considered to change from 100% to 5% of its initial value due to the compaction process.

Figure 14 represents the alteration of the Drucker-Prager criterion (η) which is defined in Equation (57) versus time. It can be observed that η in both σ_R of 33.24 and 8.31 MPa does not show an increasing trend. It can be inferred that the cement sheath at a depth of 2075 m withstands the conditions found underground due to CO_2 exposure for an indefinite length of time. In Figure 14, the porosity of the failed layers reduces from 0.1500 to 0.0375 due to the compaction process. Figure 14 is representative of trends seen in Figure 17 and Figure 18 (referred to Appendix A.). It can be understood that the radial compaction process postpones the overall failure of the cement matrix to a great extent. Changing either the porosity of the compacted layers (PoC) or the radial stress do not shorten the lifespan of the cement matrix, except at σ_R of zero and t/r of 0.06. At σ_R of zero, it is no feasible to consider the compaction process as being an active process. Because the radial compaction process is based on considering that the radial stress leads to the compaction of the failed layers of the cement sheath. However, in neither of Figure 17 nor Figure 18, does the predicted lifespan of the cement matrix fall below 1822 years. Generally, it can be concluded that the radial compaction process is advantageous to cement sheath durability.

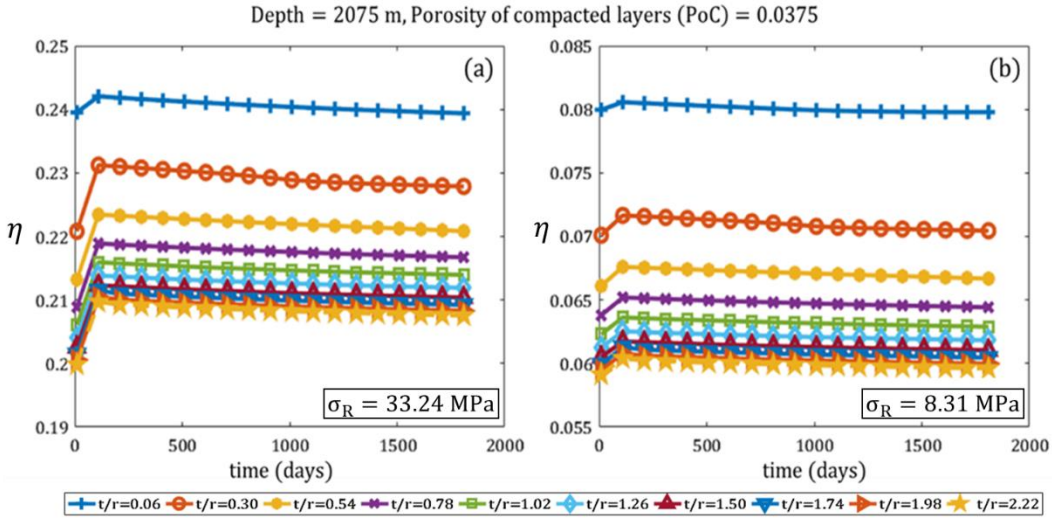

Figure 14. The profile of η (the Drucker-Prager failure criterion) versus time (days), t/r shows the ratio of the radial thickness of the cement sheath over its inside radius, the depth is 2075 m, the porosity of compacted layers (PoC) is 0.0375. (a) The radial stress (σ_R) on the outside face of the cement sheath from the surrounding rock is 33.24 MPa; (b) the radial stress is 8.31 MPa.

7 Conclusions

This study provides a framework to predict the cement lifespan under the conditions found underground. It is important to predict the failure time of well cements, because of their consequent conversion to potential CO_2 leakage pathways within a CCS concept. The CO_2

leakage through the well cements compromises the time and expense invested in CCS projects and negates their value as viable long term sequestration locations.

Abandoned oil and gas wells used for carbon capture are likely to be exposed to CO_2 due to the migration of CO_2 plumes from the injection wells. The brine as a ubiquitous component within the depleted oil and gas reservoirs reacts with the injected CO_2 to produce carbonic acid. The exposure of well cements used in the borehole or for capping to this acidic environment leads to the calcium leaching from the cement matrix. This process leads to the carbonation and degradation of the cement which endangers its durability. The durability, in this paper, is assumed to be a function of its mechanical properties. In other words, one can predict the maximum lifespan of a cement matrix based on the degradation of its mechanical properties. In this paper, to predict the lifespan of a cement matrix, a geomechanical and a geochemical process have been coupled.

In this paper, two processes are predicted to occur within a cement sheath under geosequestration conditions. Firstly, cement degradation weakens the integrity of the outermost layers within a cement sheath. These layers are prone to crack under the high overburden and low radial confining stresses. This phenomenon is referred to as the radial cracking process, which increases the vertical stress on the interior layers. In this case, the outer layers crack and act similar to a sponge with a porosity of one surrounding the interior zones. The other state occurs when the radial stress compacts the outmost layers. The compaction of these layers reduces the porosity which limits the diffusion of CO_2-bearing fluids deeper into the cement matrix. Therefore, a reasonable result is to expect a longer lifespan for the cement sheath under the influence of this phenomenon which is referred to as the radial compaction process. These two phenomena are investigated here and the following represents the significant findings of this work:

- Generally, increasing the radial thickness of the cement sheath from 6 to 222 mm around a casing with an outer radius of 88.90 mm (or an outer diameter of 7 inches) can prolong the lifespan of the cement sheath by more than 15 fold when the radial cracking process is active. In the radial compaction process, the cement lifespan increases 25 fold with increasing the radial thickness of the cement sheath. It is worth noting that the failure time for a cement sheath with a radial thickness of 26.67 mm (t/r=0.30) and at a depth of 2075 m in the radial cracking process is 158, 191, 150, 107 and 79 years at radial stresses of 0, 8.31, 16.62, 24.93, and 33.24 MPa, respectively. The lifespan of the cement sheath at depths of 800, 1225, 1650, 2075, and 2500 m is 293, 166, 112, 79, and 56 years, respectively, by considering a cement sheath with a radial thickness of 26.67 mm (t/r=0.30) and a maximum radial stress calculated at each depth using Equation (1).
- Under the condition of maximum radial stress calculated at each depth using Equation (1), the radial compaction helps the cement matrices to keep their integrity for an unlimited time (at worst cases even more than 1822 years), while, the radial cracking process shows a decrease in the lifespan of the cement matrix with increasing depth.
- When the radial cracking is active, every 425 m increase in the depth results in about a 39% decrease in the cement lifespan. In this case, the minimum time calculated for the cement failure corresponds to the depth of 2500 m, and the cement radial thickness of 6 mm which is about 37 years. In this case, it could delay CO_2 leakage at shallower depths.
- It can be observed that some of the abandoned wells during the last century which are exposed to CO_2-bearing fluids are close to their failure point from a pessimistic viewpoint. With increasing depth, the cement sheath of abandoned wells will more readily face failure when the radial cracking process is active.

This simulation considers the cement sheath surrounded by the rocks and ignores the effect of geochemical reactions on the steel casing at its outside radius. Therefore, extra work will be needed to consider the interaction of invading fluids with the steel casing. Usually, in the presence of the cement matrix, steel casings are more susceptible to rust and produce a layer of scale which prevents further degradation and penetration into the wellbore. However, the simulations in this paper do not demonstrate the penetration to the inside radius of the cement sheath. Moreover, it is worth noting that failure within the cement structure does not necessarily mean CO_2 leakage, as the failure products and dislodged surrounding rocks will probably partially fill in the gaps depending on the underground conditions which need further studies.

The numerical method applied in this simulation uses a one-step iterative method to conjugate the geochemical and the geomechanical simulation processes. In order to increase the precision and reliability of the results, it is suggested that all the geochemical and geomechanical equations are solved in one step rather than using an iterative method such as in Figure 3. Larger time steps can be applied using the implicit solution method, meaning that the simulation can predict larger time frames. In addition, this method is more stable although computationally demanding.

Acknowledgements

We would like to thank the staff at the Research Centre for Fluid and Complex System (FCS) and the Centre for Built and Natural Environment (BNE) at Coventry University for supporting us by providing constructive comments and improving the manuscript, especially Dr Philip Costen. The authors also appreciate both Centres at Coventry University for their financial support. We also thank Dr Carl Steefel for the use of CrunchFlow code.

Appendix A.

Section A.1 investigates the radial cracking process and shows the alteration in the Drucker-Prager criterion of failure, η. Section A.2 discusses the compaction process and changes in η with time when the porosity of the compacted layers reduces to a fraction of its initial value. The cement failure time is predicted by the extrapolation of the linear functions fitting over 1210 to 1810 days to η of one in Figure 15 to Figure 18 at different ratios of t/r. Figure 10 and Figure 13 are obtained based on the extrapolations of plots in Figure 15 and Figure 16, respectively.

A.1 The Radial Cracking Process

Figure 15 (a), as an example, illustrates that the Drucker-Prager failure criterion (η) increases to below 0.09 for the whole sample over 1810 days at t/r of 0.06. The magnitude of the difference between η and one is inversely related to the tendency of the cement failure. Once η of the whole cement matrix becomes greater or equal to one, the cement matrix fails. Figure 15 (a) and (b) are indirectly illustrating the cement failure tendency and change in its shape, respectively, at σ_R of zero. In this case, geochemical and geomechanical changes generally result in the porosity increase although it is not still enough for the cement failure. It is expected that the cement failure occurs after a while before the radial cracking reaches the inner radius of the cement sheath. In this process, the radial cracking process aggravates cement degradation by reducing its compressive strength.

An increase in the value of t/r decreases the slope of η versus time during the final 800 days of the simulation in Figure 15 (a), (c), (e), (g), and (i). This occurs because the CO_2-bearing fluids have a greater effect on the low-thickness cement matrices than the thick ones. At low ratios of t/r, the penetration depth of CO_2-bearing fluids is comparable with the radial thickness of the cement sheath.

Figure 15 (b), (d), (f), (h), and (j) illustrate a constant depth of penetration after the first 110 days which occurs due to the carbonation. Carbonation decreases the porosity within the calcite precipitation zone leading to an increase in the overall compressive strength. The gradual diffusion of CO_2-bearing fluids through this zone slowly depletes portlandite within the inner parts of the cement matrix. The depletion of the portlandite will be more uniform throughout the inner parts. In fact, the calcite precipitation zone acts similar to a barrier which prevents the ingress of sharp pH fronts into the inner parts. The portlandite dissolution increases the porosity and hence decreases the overall compressive strength. Clearly, this phenomenon is more effective on the low thickness cement sheaths as shown in Figure 15. The time in which the η becomes greater than one is considered as the failure time which indicates the maximum lifespan under the inured conditions.

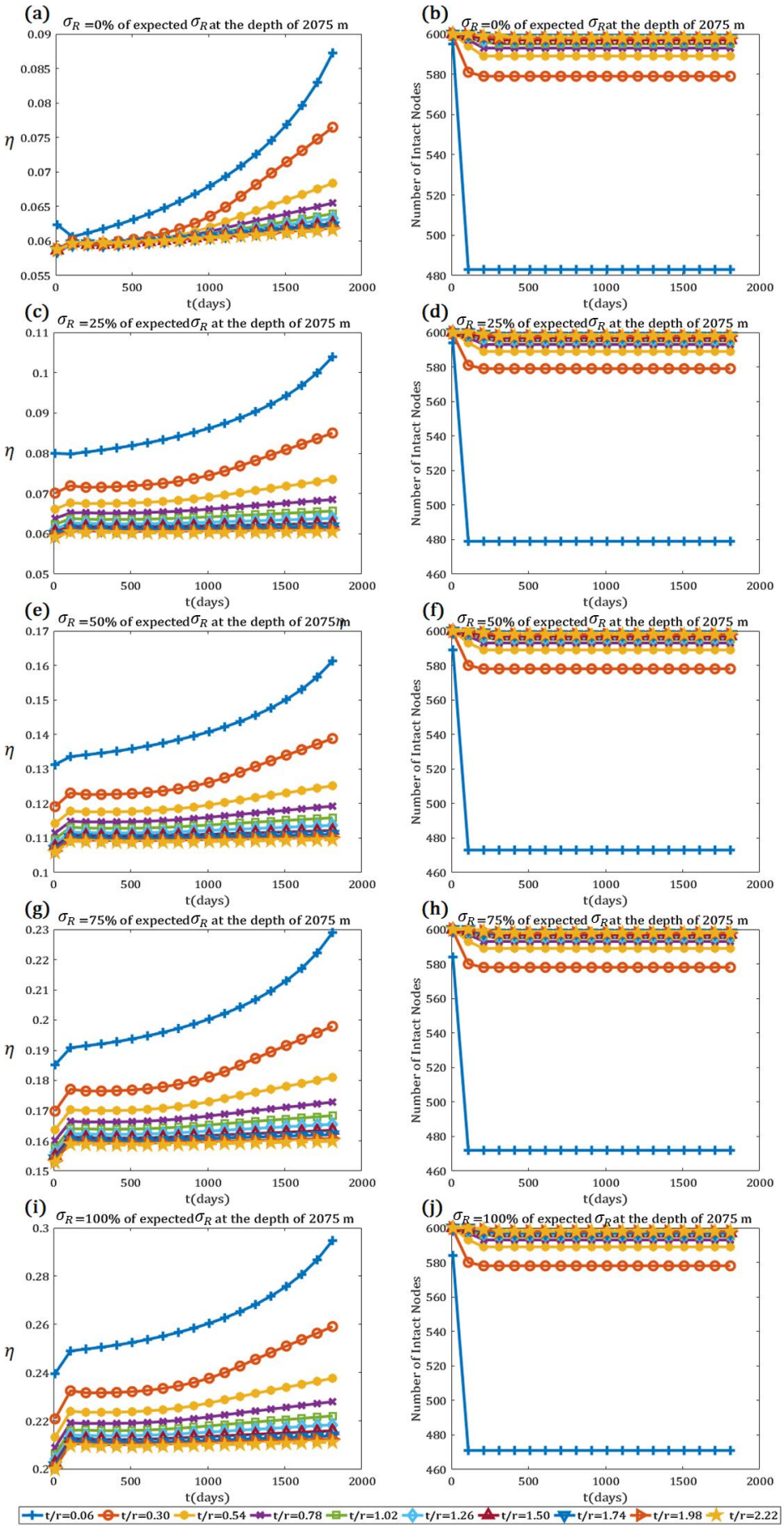
(a) σ_R =0% of expected σ_R at the depth of 2075 m
(b) σ_R =0% of expected σ_R at the depth of 2075 m
(c) σ_R =25% of expected σ_R at the depth of 2075 m
(d) σ_R =25% of expected σ_R at the depth of 2075 m
(e) σ_R =50% of expected σ_R at the depth of 2075 m
(f) σ_R =50% of expected σ_R at the depth of 2075 m
(g) σ_R =75% of expected σ_R at the depth of 2075 m
(h) σ_R =75% of expected σ_R at the depth of 2075 m
(i) σ_R =100% of expected σ_R at the depth of 2075 m
(j) σ_R =100% of expected σ_R at the depth of 2075 m
η
Number of Intact Nodes
t(days)
t/r=0.06
t/r=0.30
t/r=0.54
t/r=0.78
t/r=1.02
t/r=1.26
t/r=1.50
t/r=1.74
t/r=1.98
t/r=2.22

Figure 15. Change in the Drucker-Prager failure criterion (η), and in the number of involved nodes within the simulation out of 600 nodes at the different ratios of the radial thickness of the cement sheath over its inside radius (t/r) versus time at different radial stresses (σ_R). (a) and (b) show the trends of η and the number of uncracked or intact nodes at σ_R of 0, respectively; (c) and (d) show the trends of η and the number of intact nodes at σ_R of 8.31 MPa, respectively; (e) and (f) show the trends of η and the number of intact nodes at σ_R of 16.62 MPa, respectively; (g) and (h) show the trends of η and the number of intact nodes at σ_R of 24.93 MPa, respectively; (i) and (j) show the trends of η and the number of intact nodes at σ_R of 33.24 MPa, respectively. Depth in all plots is 2075 m, and the radial cracking is the active process.

Figure 16 shows the effect of depth on cement durability. With increasing depth, the curves of η shift upwards in this figure. It can be observed that the depth of crack penetration is not affected by increasing in depth.

The effect of carbonation is apparent in Figure 16 (b), (d), (f), (h), and (j) which shows a constant depth of penetration after the first 110 days. This phenomenon increases the cement strength in the early stages and stops the further movement of the pH front into the inner parts of the cement matrix. It is worth noting that the carbonated layer also degrades with time, therefore, the eventual reopening of this layer could be expected. However, this time period is far beyond the simulation time scale in this paper. In fact, this process is extremely slow due to the small difference between the rate of calcite precipitation and degradation.

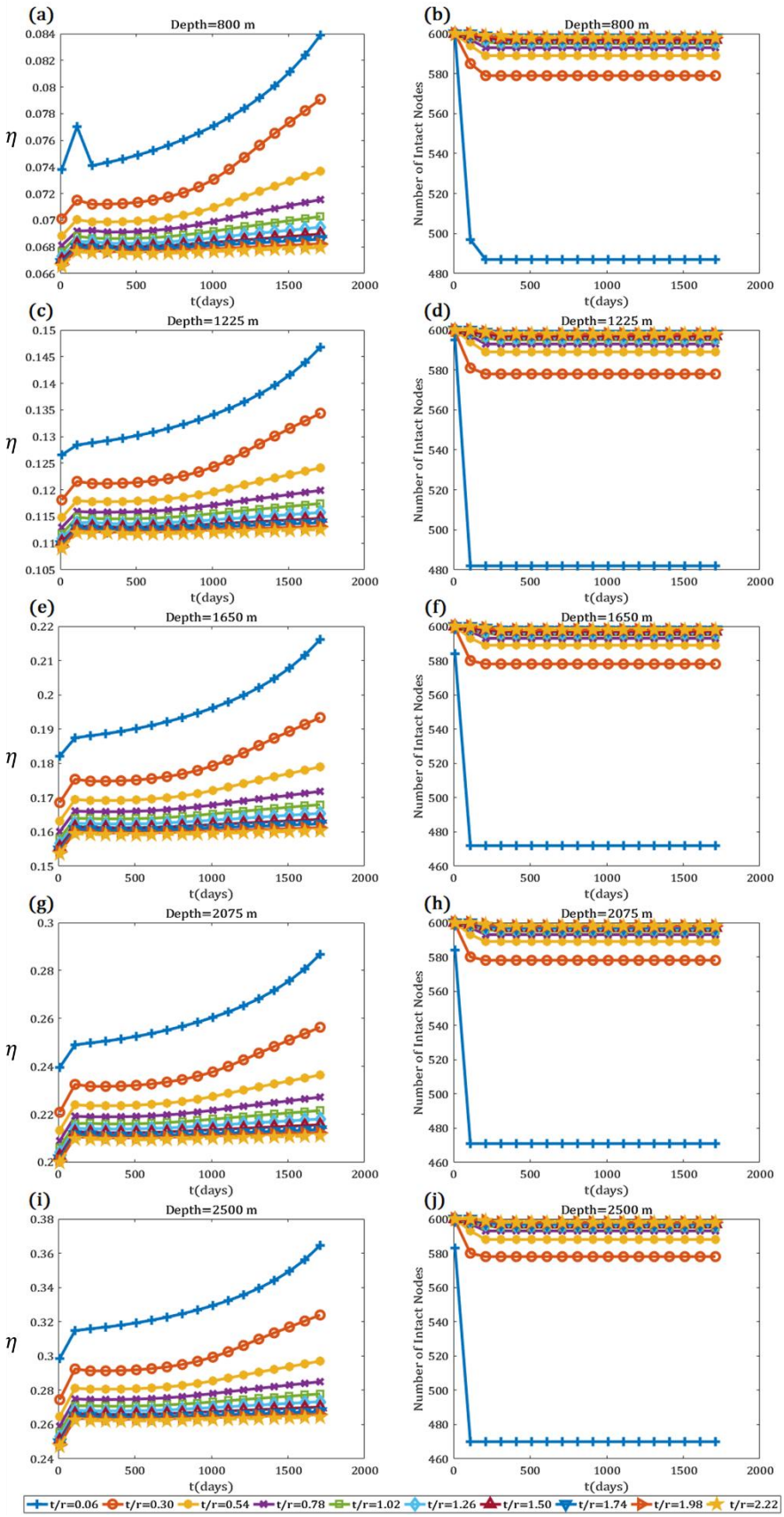

Figure 16. Change in the Drucker-Prager failure criterion (η), and change in the number of involved nodes within the simulation out of 600 nodes at the different ratios of the radial thickness of the cement sheath over its inside radius (t/r), and at different depths. (a) and (b) show the trends of η and the number of uncracked or intact nodes at the depth of 800 m, respectively; (c) and (d) show the trends of η and the

number of intact nodes at the depth of 1225 m, respectively; (e) and (f) show the trends of η and the number of intact nodes at the depth of 1650 m, respectively; (g) and (h) show the trends of η and the number of intact nodes at the depth of 2075 m, respectively; (i) and (j) show the trends of η and the number of intact nodes at the depth of 2500 m, respectively. The radial stress, in all plots, is assumed to be equal to the in-situ horizontal stress obtained from Equation (1) at each depth. The radial cracking is the active process.

A.2 The Radial Compaction Process

The compaction process is investigated at different depths of a well and the porosity of the compacted layers (PoC) in Figure 17. In this figure, the ratio of the radial thickness over the inside radius (t/r) of the cement sheath is between 0.06 and 2.22, and the depth changes from 800 to 2500 m. The zero slopes of η curves vs. time represents that at depths from 800 to 2500 m and under typical radial stresses (i.e., calculated based on Equation (1) for each depth) the cement failure is never expected to occur. In fact, the radial compaction process will preserve the cement against being degraded aggressively by CO_2-bearing fluids. Figure 17 illustrates the impact of the geomechanical changes within the cement matrix. The imposed effective stress decreases the overall porosity of the cement matrix. This alteration increases the Young's modulus of layers and the overall compressive strength of the cement matrix. Therefore, the cement matrix is strengthened which reduces the failure tendency over a short period of time.

The shortest failure time calculated in Figure 17 and **Figure 18** is about 1822 years for t/r of 0.06, σ_R of 24.93 MPa, PoC of 0.0750, and a depth of 2075 m in **Figure 18** (r). Hence, under the normal underground conditions, the radial compaction process maintains the cement matrix on the safe side.

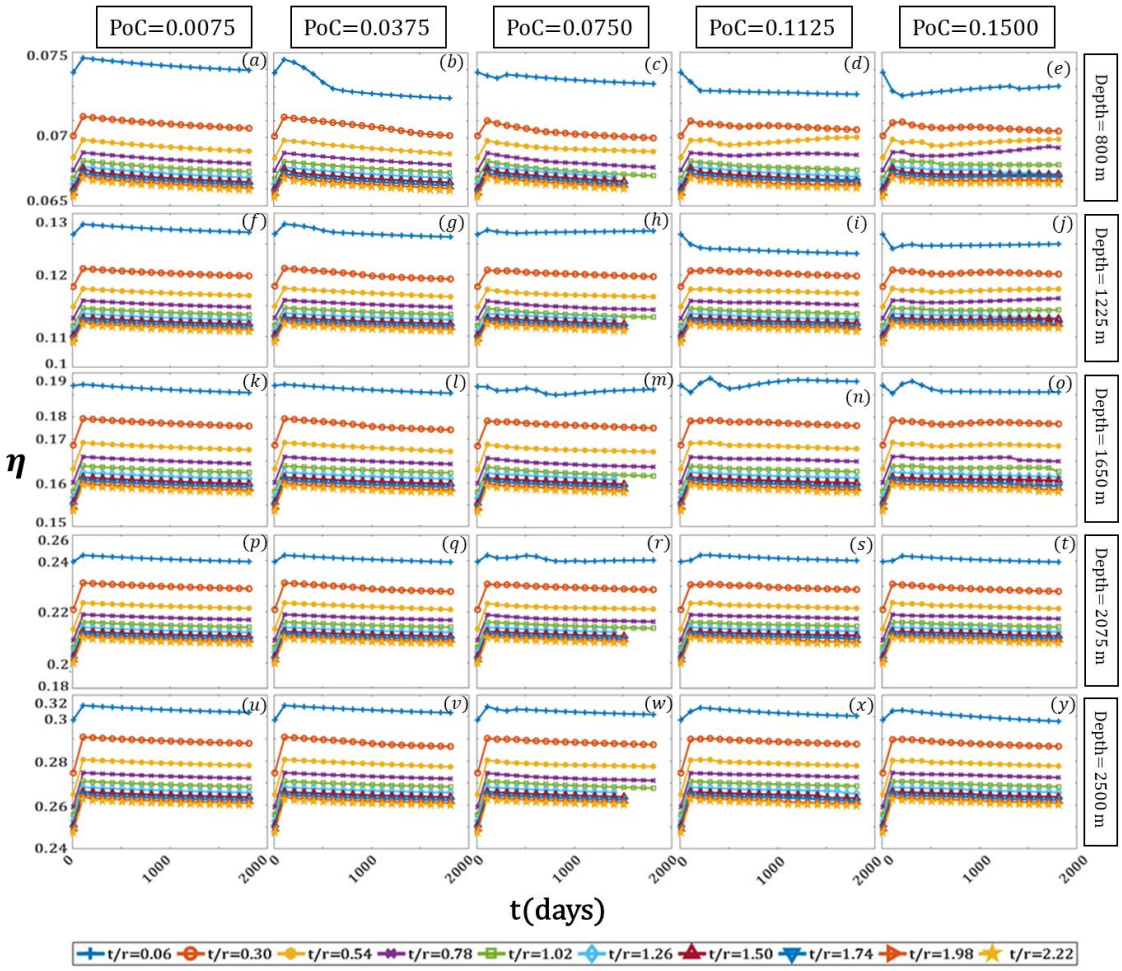

Figure 17. Change in η at different depths and ratios of the radial cement thickness over its inside radius (t/r) when the radial compaction process is active. PoC is the porosity of the compacted layer which is constant through the columns of the figure. Depth is also constant in every row. σ_R is calculated using Equation (1) at each depth.

In **Figure 18**, the radial stress changes from zero to the typical radial stress calculated using Equation (1) depending on stress conditions found underground. At depth of 2075 m, the typical radial pressure is 32.24 MPa. The effect of the radial stress on the radial compaction process is considerable, although, different PoCs illustrate a similar behaviour at constant values of σ_R as shown in rows of **Figure 18**.

A comparison of Figure 16 with Figure 17 shows that under typical radial stresses the radial compaction process can help cement to maintain its integrity for an unlimited time (at worst cases more than 1822 years). The radial cracking process illustrates that the failure tendency of the cement matrix increases with depth. This could be propitious, as the increased durability of the cement matrices at shallower depths can exponentially delay the CO_2 leakage to the Earth's surface when the radial cracking is active.

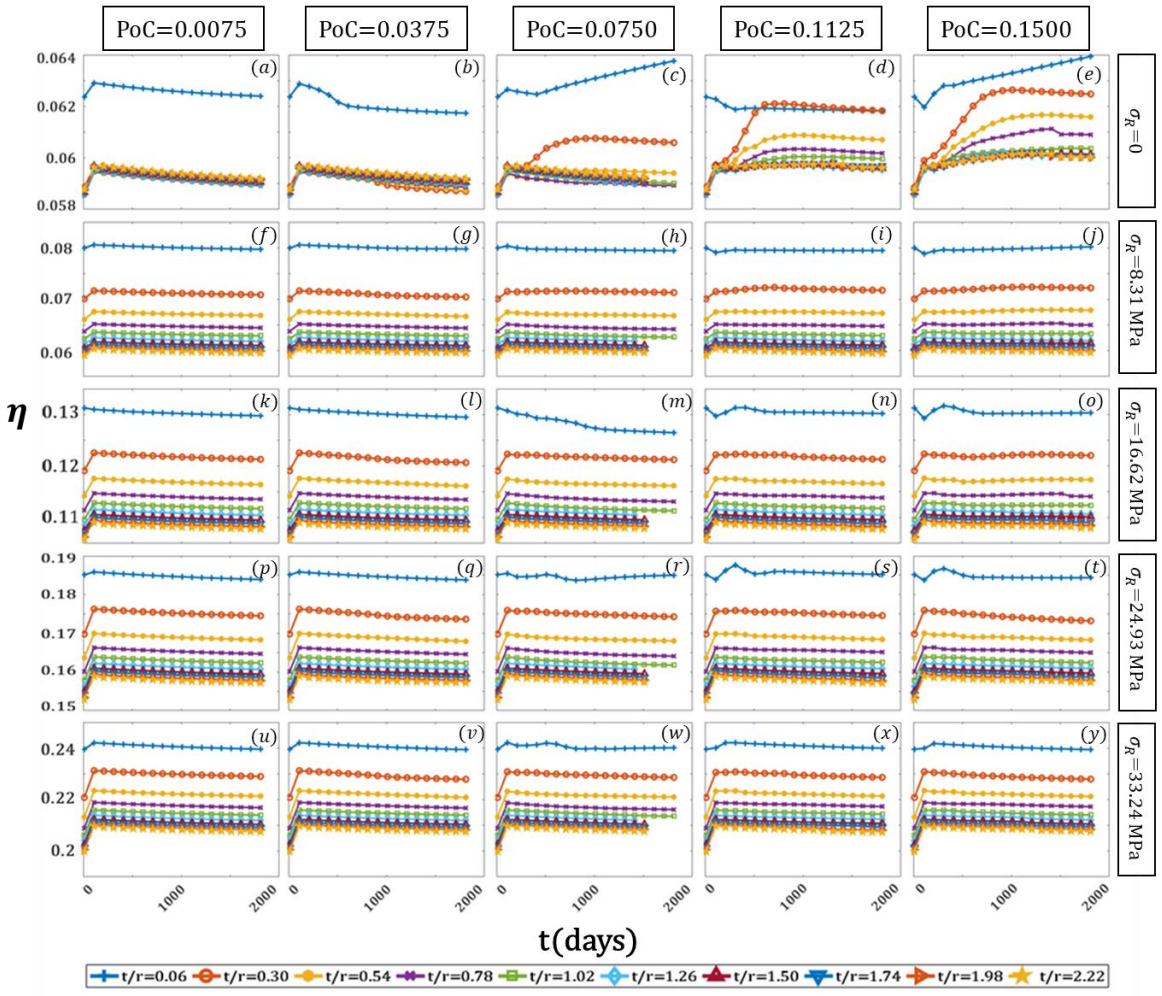

Figure 18. Change in η at different depths and ratios of the radial cement thickness over its inside radius (t/r) when the radial compaction process is active. PoC is the porosity of the compacted layer which is constant through the columns of the figure. σ_R is also constant in every row. Depth is 2075 m in all plots.

References

Abbaszadeh, M., Shariatipour, S., 2018. Investigating the Impact of Reservoir Properties and Injection Parameters on Carbon Dioxide Dissolution in Saline Aquifers. Fluids 3, 76. https://doi.org/10.3390/fluids3040076

Abdoulghafour, H., Gouze, P., Luquot, L., Leprovost, R., 2016. Characterization and modeling of the alteration of fractured class-G Portland cement during flow of CO2-rich brine. Int. J. Greenh. Gas Control 48, 155–170. https://doi.org/10.1016/j.ijggc.2016.01.032

Allen, A.J., Thomas, J.J., Jennings, H.M., 2007. Composition and density of nanoscale calcium–silicate–hydrate in cement. Nat. Mater. 6, 311–316. https://doi.org/10.1038/nmat1871

Arjomand, E., Bennett, T., Nguyen, G.D., 2018. Evaluation of cement sheath integrity subject to enhanced pressure. J. Pet. Sci. Eng. 170, 1–13. https://doi.org/10.1016/j.petrol.2018.06.013

Arıoglu, N., Girgin, Z.C., Arıoglu, E., 2006. Evaluation of ratio between splitting tensile strength and compressive strength for concretes up to 120 MPa and its application in strength criterion. ACI Mater. J. 103, 18–24.

Ashraf, W., 2016. Carbonation of cement-based materials: Challenges and opportunities. Constr. Build. Mater. 120, 558–570. https://doi.org/10.1016/j.conbuildmat.2016.05.080

Bachu, S., Bennion, D.B., 2009. Experimental assessment of brine and/or CO2 leakage through well cements at reservoir conditions. Int. J. Greenh. Gas Control 3, 494–501. https://doi.org/10.1016/j.ijggc.2008.11.002

Bagheri, M., Shariatipour, S.M., Ganjian, E., 2019. A Study on the Chemo-mechanical Alteration of Cement in CO2 Storage Sites. SPE Eur. Featur. 81st EAGE Annu. Conf. Exhib. (Accepted/, (In press).

Bagheri, M., Shariatipour, S.M., Ganjian, E., 2018. A review of oil well cement alteration in CO2-rich environments. Constr. Build. Mater. 186C, 946–968. https://doi.org/10.1016/j.conbuildmat.2018.07.250

Barlet-Gouédard, V., Rimmelé, G., Goffé, B., Porcherie, O., 2007. Well Technologies for CO 2 Geological Storage: CO 2 -Resistant Cement. Oil Gas Sci. Technol. - Rev. l'IFP 62, 325–334. https://doi.org/10.2516/ogst:2007027

Barlet-Gouédard, V., Rimmelé, G., Porcherie, O., Quisel, N., Desroches, J., 2009. A solution against well cement degradation under CO2geological storage environment. Int. J. Greenh. Gas Control 3, 206–216. https://doi.org/10.1016/j.ijggc.2008.07.005

Biot, M.A., 1955. Theory of elasticity and consolidation for a porous anisotropic solid. J. Appl. Phys. 26, 182–185. https://doi.org/10.1063/1.1721956

Breckels, I.M., van Eekelen, H.A.M., 1982. Relationship Between Horizontal Stress and Depth in Sedimentary Basins. J. Pet. Technol. 34, 2191–2199. https://doi.org/10.2118/10336-PA

Brunet, J.P.L., Li, L., Karpyn, Z.T., Huerta, N.J., 2016. Fracture opening or self-sealing: Critical residence time as a unifying parameter for cement-CO2-brine interactions. Int. J. Greenh. Gas Control 47, 25–37. https://doi.org/10.1016/j.ijggc.2016.01.024

Brunet, J.P.L., Li, L., Karpyn, Z.T., Kutchko, B.G., Strazisar, B., Bromhal, G., 2013. Dynamic evolution of cement composition and transport properties under conditions relevant to geological carbon sequestration. Energy and Fuels 27, 4208–4220. https://doi.org/10.1021/ef302023v

Calvert, D.G., Smith, D.K., Duncan, O.K., 1994. Issues and Techniques of Plugging and Abandonment of Oil and Gas Wells.

Cao, P., Karpyn, Z.T., Li, L., 2015. Self-healing of cement fractures under dynamic flow of CO 2 -rich brine. Water Resour. Res. 51, 4684–4701. https://doi.org/10.1002/2014WR016162

Carey, J.W., 2013. Geochemistry of Wellbore Integrity in CO2 Sequestration: Portland Cement-Steel-Brine-CO2 Interactions. Rev. Mineral. Geochemistry 77, 505–539. https://doi.org/10.2138/rmg.2013.77.15

Carey, J.W., Svec, R., Grigg, R., Zhang, J., Crow, W., 2010. Experimental investigation of wellbore integrity and CO2-brine flow along the casing-cement microannulus. Int. J. Greenh. Gas Control 4, 272–282. https://doi.org/10.1016/j.ijggc.2009.09.018

Carey, J.W., Wigand, M., Chipera, S.J., WoldeGabriel, G., Pawar, R., Lichtner, P.C., Wehner, S.C., Raines, M.A., Guthrie, G.D., 2007. Analysis and performance of oil well cement with 30 years of CO2 exposure from the SACROC Unit, West Texas, USA. Int. J. Greenh. Gas Control 1, 75–85. https://doi.org/10.1016/S1750-5836(06)00004-1

Carroll, S., Carey, J.W., Dzombak, D., Huerta, N.J., Li, L., Richard, T., Um, W., Walsh, S.D.C., Zhang, L., 2016. Review: Role of chemistry, mechanics, and transport on well integrity in CO2storage environments. Int. J. Greenh. Gas Control 49, 149–160. https://doi.org/10.1016/j.ijggc.2016.01.010

Carroll, S.A., Iyer, J., Walsh, S.D.C., 2017. Influence of Chemical, Mechanical, and Transport Processes on Wellbore Leakage from Geologic CO2 Storage Reservoirs. Acc. Chem. Res. 50, 1829–1837. https://doi.org/10.1021/acs.accounts.7b00094

Carter, C.B., Norton, M.G., 2007. Ceramic materials : science and engineering. Springer, pp. 290–297.

Celia, M.A., Bachu, S., Nordbotten, J.M., Kavetski, D., Gasda, S., 2006. A risk assessment modeling tool to quantify leakage potential through wells in mature sedimentary basins.

Proc. 8th Int. Conf. Greenh. Gas Control Technol. Trondheim, Norw. 1–6.
Chamrova, R., 2010. Modelling and Measurement of Elastic Properties of Hydrating Cement Paste.
Chen, J.J., Thomas, J.J., Taylor, H.F.W., Jennings, H.M., 2004. Solubility and structure of calcium silicate hydrate. Cem. Concr. Res. 34, 1499–1519. https://doi.org/10.1016/J.CEMCONRES.2004.04.034
Chindaprasirt, P., Jaturapitakkul, C., Sinsiri, T., 2005. Effect of fly ash fineness on compressive strength and pore size of blended cement paste. Cem. Concr. Compos. 27, 425–428. https://doi.org/10.1016/j.cemconcomp.2004.07.003
Choi, B.Y., Lee, H., Chae, G.T., Kim, T., Kim, J.C., 2016. Alteration processes of cement induced by CO2-saturated water and its effect on physical properties: Experimental and geochemical modeling study. Chemie der Erde - Geochemistry 76, 597–604. https://doi.org/10.1016/j.chemer.2016.10.001
Constantinides, G., Ulm, F.J., 2007. The nanogranular nature of C-S-H. J. Mech. Phys. Solids 55, 64–90. https://doi.org/10.1016/j.jmps.2006.06.003
Constantinides, G., Ulm, F.J., 2004. The effect of two types of C-S-H on the elasticity of cement-based materials: Results from nanoindentation and micromechanical modeling. Cem. Concr. Res. 34, 67–80. https://doi.org/10.1016/S0008-8846(03)00230-8
Corvisier, J., Brunet, F., Fabbri, A., Bernard, S., Findling, N., Rimmelé, G., Barlet-Gouédard, V., Beyssac, O., Goffé, B., 2010. Raman mapping and numerical simulation of calcium carbonates distribution in experimentally carbonated Portland-cement cores. Eur. J. Mineral. 22, 63–74. https://doi.org/10.1127/0935-1221/2010/0022-1977
Corvisier, J., Fabbri, A., Brunet, F., Leroy, Y., Goffé, B., Rimmelé, G., Barlet-Gouédard, V., 2013. A Numerical Model for CO 2 Wells Ageing through Water/Supercritical CO 2 /Cement Interactions, in: Thermo-Hydromechanical and Chemical Coupling in Geomaterials and Applications. John Wiley & Sons, Inc., Hoboken, NJ, USA, pp. 75–84. https://doi.org/10.1002/9781118623565.ch5
Davies, R.J., Almond, S., Ward, R.S., Jackson, R.B., Adams, C., Worrall, F., Herringshaw, L.G., Gluyas, J.G., Whitehead, M.A., 2014. Oil and gas wells and their integrity: Implications for shale and unconventional resource exploitation. Mar. Pet. Geol. 56, 239–254. https://doi.org/10.1016/J.MARPETGEO.2014.03.001
Dávila, G., Luquot, L., Soler, J.M., Cama, J., 2016. 2D reactive transport modeling of the interaction between a marl and a CO_2-rich sulfate solution under supercritical CO_2 conditions. Int. J. Greenh. Gas Control 54, 145–159. https://doi.org/10.1016/j.ijggc.2016.08.033
Deremble, L., Loizzo, M., Huet, B., Lecampion, B., Quesada, D., 2011. Stability of a leakage pathway in a cemented annulus. Energy Procedia 4, 5283–5290. https://doi.org/10.1016/j.egypro.2011.02.508
Dijk, P.E., Berkowitz, B., 1999. Characterizing flow and transport in factures geological media: A review. Adv. Water Resour. 25, 861–884. https://doi.org/10.1016/S0309-1708(02)00042-8
Druckenmiller, M.L., Maroto-Valer, M.M., 2005. Carbon sequestration using brine of adjusted pH to form mineral carbonates. Fuel Process. Technol. 86, 1599–1614. https://doi.org/10.1016/j.fuproc.2005.01.007
Drucker, D.C., Prager, W., 1952. SOIL MECHANICS AND PLASTIC ANALYSIS OR LIMIT DESIGN. Q. Appl. Math. 10, 157–165.
Duan, Z., Sun, R., 2003. An improved model calculating CO2 solubility in pure water and aqueous NaCl solutions from 273 to 533 K and from 0 to 2000 bar. Chem. Geol. 193, 257–271. https://doi.org/10.1016/S0009-2541(02)00263-2
Duguid, A., Radonjic, M., Scherer, G.W., 2011. Degradation of cement at the reservoir/cement interface from exposure to carbonated brine. Int. J. Greenh. Gas Control 5, 1413–1428. https://doi.org/10.1016/j.ijggc.2011.06.007

Duguid, A., Scherer, G.W., 2010. Degradation of oilwell cement due to exposure to carbonated brine. Int. J. Greenh. Gas Control 4, 546–560. https://doi.org/10.1016/j.ijggc.2009.11.001

Fabbri, A., Corvisier, J., Schubnel, A., Brunet, F., Goffé, B., Rimmele, G., Barlet-Gouédard, V., 2009. Effect of carbonation on the hydro-mechanical properties of Portland cements. Cem. Concr. Res. 39, 1156–1163. https://doi.org/10.1016/j.cemconres.2009.07.028

Geertsma, J., 1957. The effect of fluid pressure decline on volumetric changes of porous rocks. Trans Am Inst Min Met. Pet Eng 210, 331–340.

Geloni, C., Giorgis, T., Battistelli, A., 2011. Modeling of Rocks and Cement Alteration due to CO2Injection in an Exploited Gas Reservoir. Transp. Porous Media 90, 183–200. https://doi.org/10.1007/s11242-011-9714-0

Ghabezloo, S., Sulem, J., Guédon, S., Martineau, F., Saint-Marc, J., 2008. Poromechanical behaviour of hardened cement paste under isotropic loading. Cem. Concr. Res. 38, 1424–1437. https://doi.org/10.1016/J.CEMCONRES.2008.06.007

Gholami, R., Aadnoy, B., Fakhari, N., 2016a. Journal of Petroleum Science and Engineering A thermo-poroelastic analytical approach to evaluate cement sheath integrity in deep vertical wells. J. Pet. Sci. Eng. 147, 536–546. https://doi.org/10.1016/j.petrol.2016.09.024

Gholami, R., Rasouli, V., Aadnoy, B., Mohammadnejad, M., 2016b. Geomechanical and numerical studies of casing damages in a reservoir with solid production. Rock Mech. Rock Eng. 49, 1441–1460. https://doi.org/10.1007/s00603-015-0828-5

Haghi, R.K., Chapoy, A., Peirera, L.M.C., Yang, J., Tohidi, B., 2017. pH of CO 2 saturated water and CO 2 saturated brines: Experimental measurements and modelling. Int. J. Greenh. Gas Control 66, 190–203. https://doi.org/10.1016/j.ijggc.2017.10.001

Harrold, T.W.D., 2001. Porosity and e ective stress relationships in mudrocks Porosity and effective stress relationships in By.

Harsh, S., Shen, Z., Darwin, D., 1990. Strain-rate sensitive behavior of cement paste and mortar in compression. ACI Mater. J. 87, 508–516. https://doi.org/10.14359/1931

Herzog, H., Golomb, D. a N., 2004. Carbon Capture and Storage from Fossil Fuel Use. Encycl. Energy 1, 1–11. https://doi.org/http://dx.doi.org/10.1016/B0-12-176480-X/00422-8

Hill, R., 1952. the Elastic Behaviour of a Crystalline Aggregate. Proc. Phys. Soc. London Sect. A 65, 349–355. https://doi.org/10.1088/0370-1298/65/5/307

Hoek, E., Brown, E.T., 1997. Practical estimates of rock mass strength. Int. J. Rock Mech. Min. Sci. 34, 1165–1186. https://doi.org/10.1016/S1365-1609(97)80069-X

Hopcroft, M.A., Nix, W.D., Kenny, T.W., 2010. What is the Young's Modulus of Silicon? J. MICROELECTROMECHANICAL Syst. 19. https://doi.org/10.1109/JMEMS.2009.2039697

Huerta, N.J., Bryant, S.L., Conrad, L., 2008. Cement Core Experiments With A Conductive Leakage Pathway , Under Confining Stress And Alteration Of Cement ' s Mechanical Properties Via A Reactive Fluid , As An Analog For CO2 Leakage Scenario. SPE/DOE Improv. Oil Recover. Symp. Tulsa, Oklahoma, 19-23 April SPE-113375. https://doi.org/10.2118/113375-MS

Huerta, N.J., Bryant, S.L., Strazisar, B.R., Kutchko, B.G., Conrad, L.C., 2009. The influence of confining stress and chemical alteration on conductive pathways within wellbore cement. Energy Procedia 1, 3571–3578. https://doi.org/10.1016/j.egypro.2009.02.151

Huerta, N.J., Hesse, M.A., Bryant, S.L., Strazisar, B.R., Lopano, C., 2016. CO2-saturated water in a cement fracture : Application to wellbore leakage during geologic CO2 storage 44, 276–289.

Huerta, N.J., Hesse, M.A., Bryant, S.L., Strazisar, B.R., Lopano, C.L., 2013. Experimental evidence for self-limiting reactive flow through a fractured cement core: Implications for time-dependent wellbore leakage. Environ. Sci. Technol. 47, 269–275. https://doi.org/10.1021/es3013003

Huet, B.M., Prevost, J.H., Scherer, G.W., 2010. Quantitative reactive transport modeling of Portland cement in CO2-saturated water. Int. J. Greenh. Gas Control 4, 561–574.

https://doi.org/10.1016/j.ijggc.2009.11.003
Hwang, J., Ahmed, R., Tale, S., Shah, S., 2018. Shear bond strength of oil well cement in carbonic acid environment. J. CO2 Util. 27, 60–72. https://doi.org/10.1016/j.jcou.2018.07.001
Hyvert, N., Sellier, A., Duprat, F., Rougeau, P., Francisco, P., 2010. Dependency of C-S-H carbonation rate on CO2 pressure to explain transition from accelerated tests to natural carbonation. Cem. Concr. Res. 40, 1582–1589. https://doi.org/10.1016/j.cemconres.2010.06.010
Iyer, J., Walsh, S.D.C., Hao, Y., Carroll, S.A., 2017. Incorporating reaction-rate dependence in reaction-front models of wellbore-cement/carbonated-brine systems. Int. J. Greenh. Gas Control 59, 160–171. https://doi.org/10.1016/j.ijggc.2017.01.019
Jennings, H.M., 2000. Model for the microstructure of calcium silicate hydrate in cement paste. Cem. Concr. Res. 30, 101–116. https://doi.org/10.1016/S0008-8846(99)00209-4
Jennings, H.M., Thomas, J.J., Gevrenov, J.S., Constantinides, G., Ulm, F.J., 2007. A multi-technique investigation of the nanoporosity of cement paste. Cem. Concr. Res. 37, 329–336. https://doi.org/10.1016/j.cemconres.2006.03.021
Jo, H., Gray, K.E., 2010. Mechanical Behavior of Concentric Casing, Cement, And Formation Using Analytical And Numerical Methods.
Kari, O.P., Puttonen, J., Skantz, E., 2014. Reactive transport modelling of long-term carbonation. Cem. Concr. Compos. 52, 42–53. https://doi.org/10.1016/j.cemconcomp.2014.05.003
Kiehl, J.T., Trenberth, K.E., 1997. Earth's Annual Global Mean Energy Budget. Bull. Am. Meteorol. Soc. 78, 5. https://doi.org/10.1175/1520-0477(1997)078<0197:EAGMEB>2.0.CO;2
Kutchko, B.G., Strazisar, B.R., Dzombak, D.A., Lowry, G. V, Thaulow, N., 2007. Degradation of Well Cement by CO2 under Geological Sequestration Conditions. Env. Sci Technol 41, 4787–4792. https://doi.org/10.1021/es062828c
Kutchko, B.G., Strazisar, B.R., Huerta, N., Lowry, G. V., Dzombak, D.A., Thaulow, N., 2009. CO2 reaction with hydrated class H well cement under geologic sequestration conditions: Effects of flyash admixtures. Environ. Sci. Technol. 43, 3947–3952. https://doi.org/10.1021/es803007e
Kutchko, B.G., Strazisar, B.R., Lowry, G.V., Dzombak, D. a., Thaulow, N., 2008. Rate of CO2 Attack on Hydrated Class H Well Cement under Geologic Sequestration Conditions. Environ. Sci. \& Technol. 42, 6237–6242. https://doi.org/10.1021/es800049r
Lafhaj, Z., Goueygou, M., Djerbi, A., Kaczmarek, M., 2006. Correlation between porosity, permeability and ultrasonic parameters of mortar with variable water / cement ratio and water content. Cem. Concr. Res. 36, 625–633. https://doi.org/10.1016/j.cemconres.2005.11.009
Lecampion, B., Vanzo, J., Ulm, F.-J., Huet, B., Germay, C., Khalfallah, I., Dirrenberger, J., 2011. Evolution of Portland Cement Mechanical Properties Exposed To Co2-Rich Fluids: Investigation At Different Scales. MPPS 2011, Symp. Mech. Phys. Porous Solids A Tribut. to Pr. Oliv. Coussy 1–24.
Lesti, M., Tiemeyer, C., Plank, J., 2013. CO2stability of Portland cement based well cementing systems for use on carbon capture & storage (CCS) wells. Cem. Concr. Res. 45, 45–54. https://doi.org/10.1016/j.cemconres.2012.12.001
Li, Y.X., Chen, Y.M., Wei, J.X., He, X.Y., Zhang, H.T., Zhang, W.S., 2006. A study on the relationship between porosity of the cement paste with mineral additives and compressive strength of mortar based on this paste. Cem. Concr. Res. 36, 1740–1743. https://doi.org/10.1016/j.cemconres.2004.07.007
Lian, C., Zhuge, Y., Beecham, S., 2011. The relationship between porosity and strength for porous concrete. Constr. Build. Mater. 25, 4294–4298. https://doi.org/10.1016/j.conbuildmat.2011.05.005
Liaudat, J., Martínez, A., López, C.M., Carol, I., 2018. Modelling acid attack of oilwell cement exposed to carbonated brine. Int. J. Greenh. Gas Control 68, 191–202.

https://doi.org/10.1016/j.ijggc.2017.11.015
Liteanu, E., Spiers, C.J., 2011. Fracture healing and transport properties of wellbore cement in the presence of supercritical CO2. Chem. Geol. 281, 195–210. https://doi.org/10.1016/j.chemgeo.2010.12.008
Liu, B., Feng, X., Zhang, S.M., 2009. The effective Young's modulus of composites beyond the Voigt estimation due to the Poisson effect. Compos. Sci. Technol. 69, 2198–2204. https://doi.org/10.1016/j.compscitech.2009.06.004
Liu, S., Harpalani, S., 2014. Determination of the effective stress law for deformation in coalbed methane reservoirs. Rock Mech. Rock Eng. 47, 1809–1820. https://doi.org/10.1007/s00603-013-0492-6
Lubarda, V.A., Mastilovic, S., Knap, J., 2002. Brittle-Ductile Transition in Porous Rocks by Cap Model. J. Eng. Mech. 122, 633–642. https://doi.org/10.1061/(asce)0733-9399(1996)122:7(633)
Mainguy, M., Ulm, F., 2001. Coupled Diffusion-Dissolution Around a Fracture Channel : The Solute Congestion Phenomenon. Transp. Porous Media 45, 481–497. https://doi.org/10.1023/A:1012096014084
Mason, H.E., Du Frane, W.L., Walsh, S.D.C., Dai, Z., Charnvanichborikarn, S., Carroll, S.A., 2013. Chemical and mechanical properties of wellbore cement altered by CO 2-rich brine using a multianalytical approach. Environ. Sci. Technol. 47, 1745–1752. https://doi.org/10.1021/es3039906
McLean, M.R., Addis, M.A., 1990. Wellbore Stability: The Effect of Strength Criteria on Mud Weight Recommendations. SPE Annu. Tech. Conf. Exhib. https://doi.org/10.2118/20405-MS
McLintock, I.S., 1967. The Elovich Equation in Chemisorption Kinetics. Nature 216, 1204–1205. https://doi.org/10.1038/2161204a0
Merkel, C., Deuschle, J., Griesshaber, E., Enders, S., Steinhauser, E., Hochleitner, R., Brand, U., Schmahl, W.W., 2009. Mechanical properties of modern calcite- (Mergerlia truncata) and phosphate-shelled brachiopods (Discradisca stella and Lingula anatina) determined by nanoindentation. J. Struct. Biol. 168, 396–408. https://doi.org/10.1016/J.JSB.2009.08.014
Moner-Girona, M., Roig, A., Molins, E., Martínez, E., Esteve, J., 1999. Micromechanical properties of silica aerogels. Appl. Phys. Lett. 75, 653–655. https://doi.org/10.1063/1.124471
Nakano, K., Ohbuchi, A., Mito, S., Xue, Z., 2014. Chemical interaction of well composite samples with supercritical CO2 along the cement - Sandstone interface. Energy Procedia 63, 5754–5761. https://doi.org/10.1016/j.egypro.2014.11.608
Nelson, E.B., 1990. Well cementing. Elsevier, pp. 28–44.
Newell, A.J., Shariatipour, S.M., 2016. Linking outcrop analogue with flow simulation to reduce uncertainty in sub-surface carbon capture and storage: an example from the Sherwood Sandstone Group of the Wessex Basin, UK. Geol. Soc. London, Spec. Publ. 436, 231 LP-246. https://doi.org/10.1144/SP436.2
Nur, A., Byerlee, J.D., 1971. An exact effective stress law for elastic deformation of rock with fluids. J. Geophys. Res. 76, 6414–6419. https://doi.org/10.1029/JB076i026p06414
Nygård, R., Gutierrez, M., Bratli, R.K., Høeg, K., 2006. Brittle-ductile transition, shear failure and leakage in shales and mudrocks. Mar. Pet. Geol. 23, 201–212. https://doi.org/10.1016/j.marpetgeo.2005.10.001
Omosebi, O., Maheshwari, H., Ahmed, R., Shah, S., Osisanya, S., 2017. Experimental study of the effects of CO2concentration and pressure at elevated temperature on the mechanical integrity of oil and gas well cement. J. Nat. Gas Sci. Eng. 44, 299–313. https://doi.org/10.1016/j.jngse.2017.04.009
Omosebi, O., Maheshwari, H., Ahmed, R., Shah, S., Osisanya, S., Hassani, S., DeBruijn, G., Cornell, W., Simon, D., 2016. Degradation of well cement in HPHT acidic environment:

Effects of CO2concentration and pressure. Cem. Concr. Compos. 74, 54–70. https://doi.org/10.1016/j.cemconcomp.2016.09.006

Omosebi, O., Maheshwari, H., Ahmed, R., Shah, S., Osisanya, S., Santra, A., Saasen, A., 2015. Investigating temperature effect on degradation of well cement in HPHT carbonic acid environment. J. Nat. Gas Sci. Eng. 26, 1344–1362. https://doi.org/10.1016/j.jngse.2015.08.018

Onoja, M.U., Shariatipour, S.M., 2018. The impact of gradational contact at the reservoir-seal interface on geological CO2storage capacity and security. Int. J. Greenh. Gas Control 72, 1–13. https://doi.org/10.1016/j.ijggc.2018.03.007

Onoja, M.U., Williams, J.D.O., Vosper, H., Shariatipour, S.M., 2019. Effect of sedimentary heterogeneities in the sealing formation on predictive analysis of geological CO 2 storage. Int. J. Greenh. Gas Control 82, 229–243. https://doi.org/10.1016/j.ijggc.2019.01.013

Osipov, V.I., 2015. Physicochemical theory of effective stress in soils. Physicochem. Theory Eff. Stress Soils 1–55. https://doi.org/10.1007/978-3-319-20639-4

Peter, M.A., Muntean, A., Meier, S.A., Böhm, M., 2008. Competition of several carbonation reactions in concrete: A parametric study. Cem. Concr. Res. 38, 1385–1393. https://doi.org/10.1016/j.cemconres.2008.09.003

Phani, K.K., Niyogi, S.K., 1987. Young's modulus of porous brittle solids. J. Mater. Sci. 22, 257–263. https://doi.org/10.1007/BF01160581

Phung, Q.T., Maes, N., Jacques, D., De Schutter, G., Ye, G., Perko, J., 2016. Modelling the carbonation of cement pastes under a CO2pressure gradient considering both diffusive and convective transport. Constr. Build. Mater. 114, 333–351. https://doi.org/10.1016/j.conbuildmat.2016.03.191

Rackley, S.A., 2017. Carbon capture and storage. p. 432.

Raoof, A., Nick, H.M., Wolterbeek, T.K.T., Spiers, C.J., 2012. Pore-scale modeling of reactive transport in wellbore cement under CO2 storage conditions. Int. J. Greenh. Gas Control 11, 67–77. https://doi.org/10.1016/j.ijggc.2012.09.012

Rezagholilou, A., Papadakis, V.G., Nikraz, H., 2017. Rate of carbonation in cement modified base course material. Constr. Build. Mater. 150, 646–652. https://doi.org/10.1016/j.conbuildmat.2017.05.226

Rice, S.A., 2005. Advances in chemical physics. Volume 131. Wiley, p. 148.

Rimmelé, G., Barlet-Gouédard, V., Porcherie, O., Goffé, B., Brunet, F., 2008. Heterogeneous porosity distribution in Portland cement exposed to CO2-rich fluids. Cem. Concr. Res. 38, 1038–1048. https://doi.org/10.1016/j.cemconres.2008.03.022

Rochette, P., Labossiere, P., 1996. A Plasticity Approach for Concrete Columns Confined with Composite Materials. Adv. Compos. Mater. Bridg. Struct. -INTERNATIONAL Conf. 359–366.

Sadd, M.H., 2005. Elasticity. Theory, Applications, and Numerics.

Salamon, S., 1996. Differential Equations and Discrete Mathematics.

Šavija, B., Luković, M., 2016. Carbonation of cement paste: Understanding, challenges, and opportunities. Constr. Build. Mater. 117, 285–301. https://doi.org/10.1016/j.conbuildmat.2016.04.138

Shariatipour, S.M., Mackay, E.J., Pickup, G.E., 2016. An engineering solution for CO2 injection in saline aquifers. Int. J. Greenh. Gas Control 53, 98–105. https://doi.org/10.1016/j.ijggc.2016.06.006

Shariatipour, S.M., Pickup, G.E., Mackay, E.J., 2016. Simulations of CO2 storage in aquifer models with top surface morphology and transition zones. Int. J. Greenh. Gas Control 54, 117–128. https://doi.org/10.1016/J.IJGGC.2016.06.016

Shariatipour, S.M., Pickup, G.E., Mackay, E.J., 2014. The Effect of Aquifer/Caprock Interface on Geological Storage of CO2. Energy Procedia 63, 5544–5555. https://doi.org/10.1016/J.EGYPRO.2014.11.588

Shen, J., Dangla, P., Thiery, M., 2013. Reactive transport modeling of CO2 through cementitious materials under CO2 geological storage conditions. Int. J. Greenh. Gas Control 18, 75–87. https://doi.org/10.1016/j.ijggc.2013.07.003

Shepard, D., 1968. A two-dimensional interpolation function for irregularly-spaced data. Proc. 1968 23rd ACM Natl. Conf. - 517–524. https://doi.org/10.1145/800186.810616

Silva, A., Neves, R., De Brito, J., 2014. Statistical modelling of carbonation in reinforced concrete. Cem. Concr. Compos. 50, 73–81. https://doi.org/10.1016/j.cemconcomp.2013.12.001

Skempton, A.W., 1984. Effective Stress in Soils, Concrete and Rocks, in: SELECTED PAPERS ON SOIL MECHANICS. Thomas Telford Publishing, pp. 106–118. https://doi.org/10.1680/sposm.02050.0014

Spycher, N., Pruess, K., Ennis-King, J., 2003. CO2-H2O mixtures in the geological sequestration of CO2. I. Assessment and calculation of mutual solubilities from 12 to 100°C and up to 600 bar. Geochim. Cosmochim. Acta 67, 3015–3031. https://doi.org/10.1016/S0016-7037(03)00273-4

Steefel, C.I., Appelo, C.A.J., Arora, B., Jacques, D., Kalbacher, T., Kolditz, O., Lagneau, V., Lichtner, P.C., Mayer, K.U., Meeussen, J.C.L., Molins, S., Moulton, D., Shao, H., Šimůnek, J., Spycher, N., Yabusaki, S.B., Yeh, G.T., 2015. Reactive transport codes for subsurface environmental simulation, Computational Geosciences. https://doi.org/10.1007/s10596-014-9443-x

Stocker, T.F., Plattner, G.-K., Tignor, M.M.B., Allen, S.K., Boschung, J., Nauels, A., Xia, Y., Bex, V., Midgley, P.M., 2013. Climate Change 2013. https://doi.org/10.1017/CBO9781107415324.Summary

Ta, V.-L., Bonnet, S., Senga Kiesse, T., Ventura, A., 2016. A new meta-model to calculate carbonation front depth within concrete structures. Constr. Build. Mater. 129, 172–181. https://doi.org/10.1016/J.CONBUILDMAT.2016.10.103

Taylor, H.F.W., 1997. Cement chemistry. T. Telford, p. 123.

Terzaghi, K., 1943. Theoretical Soil Mechanics. https://doi.org/10.1002/9780470172766

Thomas, J.J., Jennings, H.M., Allen, A.J., 2010. Relationships between Composition and Density of Tobermorite, Jennite, and Nanoscale CaO–SiO 2 –H 2 O. J. Phys. Chem. C 114, 7594–7601. https://doi.org/10.1021/jp910733x

Urbonas, L., Leno, V., Heinz, D., 2016. Effect of carbonation in supercritical CO2on the properties of hardened cement paste of different alkalinity. Constr. Build. Mater. 123, 704–711. https://doi.org/10.1016/j.conbuildmat.2016.07.040

Velez, K., Maximilien, S., Damidot, D., Fantozzi, G., Sorrentino, F., 2001. Determination by nanoindentation of elastic modulus and hardness of pure constituents of Portland cement clinker. Cem. Concr. Res. 31, 555–561. https://doi.org/10.1016/S0008-8846(00)00505-6

Walsh, S.D.C., Du Frane, W.L., Mason, H.E., Carroll, S.A., 2013. Permeability of wellbore-cement fractures following degradation by carbonated brine. Rock Mech. Rock Eng. 46, 455–464. https://doi.org/10.1007/s00603-012-0336-9

Walsh, S.D.C., Mason, H.E., Du Frane, W.L., Carroll, S.A., 2014a. Mechanical and hydraulic coupling in cement-caprock interfaces exposed to carbonated brine. Int. J. Greenh. Gas Control 25, 109–120. https://doi.org/10.1016/j.ijggc.2014.04.001

Walsh, S.D.C., Mason, H.E., Du Frane, W.L., Carroll, S.A., 2014b. Experimental calibration of a numerical model describing the alteration of cement/caprock interfaces by carbonated brine. Int. J. Greenh. Gas Control 22, 176–188. https://doi.org/10.1016/j.ijggc.2014.01.004

Wang, W., Taleghani, A.D., 2014. Three-dimensional analysis of cement sheath integrity around Wellbores. J. Pet. Sci. Eng. 121, 38–51. https://doi.org/10.1016/j.petrol.2014.05.024

Wang, X., Subramaniam, K. V., 2011. Ultrasonic monitoring of capillary porosity and elastic properties in hydrating cement paste. Cem. Concr. Compos. 33, 389–401. https://doi.org/10.1016/J.CEMCONCOMP.2010.11.001

Watson, T.L., Bachu, S., 2007. Evaluation of the Potential for Gas and CO2 Leakage Along Wellbores. E&P Environ. Saf. Conf. 115–126. https://doi.org/10.2118/106817-MS

Wigand, M., Kaszuba, J.P., Carey, J.W., Hollis, W.K., 2009. Geochemical effects of CO2 sequestration on fractured wellbore cement at the cement/caprock interface. Chem. Geol. 265, 122–133. https://doi.org/10.1016/j.chemgeo.2009.04.008

Wolterbeek, T.K.T., Hangx, S.J.T., Spiers, C.J., 2016a. Effect of CO2-induced reactions on the mechanical behaviour of fractured wellbore cement. Geomech. Energy Environ. 7, 26–46. https://doi.org/10.1016/j.gete.2016.02.002

Wolterbeek, T.K.T., Peach, C.J., Raoof, A., Spiers, C.J., 2016b. Reactive transport of CO2-rich fluids in simulated wellbore interfaces: Flow-through experiments on the 1–6 m length scale. Int. J. Greenh. Gas Control 54, 96–116. https://doi.org/10.1016/j.ijggc.2016.08.034

Wong, T.F., Baud, P., 1999. Mechanical compaction of porous sandstone. Oil Gas Sci. Technol. 54, 715–727. https://doi.org/10.2516/ogst:1999061

Xu, H., Ma, T., Peng, N., Yang, B., 2018. Influences of Fracturing Fluid Injection on Mechanical Integrity of Cement Sheath under Four Failure Modes. Energies 11, 3534. https://doi.org/10.3390/en11123534

Yu, M., Chenevert, M.E., Sharma, M.M., 2003. Chemical-mechanical wellbore instability model for shales: Accounting for solute diffusion. J. Pet. Sci. Eng. 38, 131–143. https://doi.org/10.1016/S0920-4105(03)00027-5

Zhang, L., Dzombak, D.A., Nakles, D. V., Brunet, J.P.L., Li, L., 2013. Reactive transport modeling of interactions between acid gas (CO 2 + H2S) and pozzolan-amended wellbore cement under geologic carbon sequestration conditions. Energy and Fuels 27, 6921–6937. https://doi.org/10.1021/ef401749x

Zhang, L., Yan, X., Yang, X., Zhao, X., 2015. Evaluation of wellbore integrity for HTHP gas wells under solid-temperature coupling using a new analytical model. J. Nat. Gas Sci. Eng. 25, 347–358. https://doi.org/10.1016/j.jngse.2015.05.023

Zhang, M., Bachu, S., 2011. Review of integrity of existing wells in relation to CO2geological storage: What do we know? Int. J. Greenh. Gas Control 5, 826–840. https://doi.org/10.1016/j.ijggc.2010.11.006

Zhang, Q., 2016. Mathematical modeling and numerical study of carbonation in porous concrete materials. Appl. Math. Comput. 281, 16–27. https://doi.org/10.1016/j.amc.2016.01.034

Zhang, Z., Wang, H., 2017. Effect of thermal expansion annulus pressure on cement sheath mechanical integrity in HPHT gas wells. Appl. Therm. Eng. 118, 600–611. https://doi.org/10.1016/j.applthermaleng.2017.02.075

Zhu, H.X., Fan, T.X., Zhang, D., 2015. Composite materials with enhanced dimensionless Young's modulus and desired Poisson's ratio, in: Scientific Reports. Nature Publishing Group, pp. 1–8. https://doi.org/10.1038/srep14103